

Bachelor's Thesis

Properties of giant radio galaxies in the GAMA23 field

Department of Physics and Earth Sciences
Universität Leipzig



Mokessh Kannah Ciwan

Leipzig, October 28th, 2022

First supervisor: Dr. Sebastien Pezzagna
Second supervisor: Dr. Gülay Gürkan Uygun

Submitted in partial fulfilment of the requirements for the degree of B. Sc.

Abstract

Giant radio galaxies (GRG) are a subgroup of active galactic nuclei (AGN) that display incredible radio jets that extend well beyond their host galaxies (>0.7 Mpc). Similar to typical-size AGN, these radio jets are produced by the accretion of matter onto the supermassive black holes (SMBH) in the galaxy's core. However, the sheer size of the jets seen in GRGs raises some questions about the nature of these objects as well as their environments. By comparing different properties of GRGs with that of typical-size AGN, we might be able to identify the nature of their central engines and host galaxies to determine if they are intrinsically different from other AGN.

With this motivation, I combined the following data sets: (i) the radio data and the value-added radio catalogue from the Australian Square Kilometre Array Pathfinder (ASKAP) survey of the GAMA23 field, which was carried as part of the Evolutionary Map of Universe Early Science Program and (ii) the optical spectroscopy and the multi-wavelength data from optical to far-IR provided by the Galaxy and Mass Assembly Survey, to investigate the giant radio galaxies in the GAMA23 field. To identify these GRGs, I used their angular sizes and redshifts to calculate the physical sizes of their jets. Sources with jets larger than 0.7 Mpc were then considered GRGs. To identify typical-size AGN, I used the mid-infrared AllWISE colours, applying a colour cut at $W1-W2 \geq 0.7$ for AGN. A total of **63** GRGs and **5217** WISE AGN were identified using these methods.

To shed some light on the nature of GRGs, I compared multiple properties of the samples such as their angular sizes, multi-wavelength colours and luminosities, star formation rates, and stellar masses. From my analysis, the optical and near-infrared luminosities of the sources indicate that GRGs show a redder stellar population than typical-size AGN, which also supports the result that GRGs show lower star formation rates for similar stellar masses compared to typical-size AGN. Additionally, GRGs show different morphologies than typical-size AGN. GRGs are mostly hosted by elliptical galaxies whereas typical-size AGN mostly reside in spiral galaxies. I also performed a Kolmogorov–Smirnov test (K-S test) to compare these GRGs and typical-size AGN using their star formation rates and stellar masses. The analysis showed that null hypothesis (i.e. that the both samples are drawn from the same distribution) is rejected at 95% confidence level indicating that GRGs are indeed intrinsically different from typical-size AGN, based on the samples and data used in this analysis.

Contents

List of Figures	III
List of Tables	IV
1 Introduction	1
2 Active Galactic Nuclei	2
2.1 History of AGN discovery	2
2.2 AGN Structure	3
2.3 Unification models and AGN Taxonomy	5
2.3.1 Unification Models	5
2.3.2 Seyfert galaxies	7
2.3.3 LINERs	9
2.3.4 Quasars	9
2.3.5 Blazars	9
2.3.6 Radio galaxies	10
2.3.7 Giant Radio Galaxies	12
3 Data	15
3.1 Radio Data	15
3.2 Multi-wavelength Data	16
4 Analysis and discussion	18
4.1 Sample Selection	18
4.1.1 GRG selection	18
4.1.2 Typical-size AGN selection	18
4.2 Evaluation of GRG sample	21
4.2.1 Ambiguous cases	21
4.3 Comparison with WISE AGN	24
4.3.1 Angular Size	24
4.3.2 Host galaxy properties	25
4.4 Comparison to the literature	29
5 Summary and conclusion	31
6 References	33
A Appendix	V
A.1 Postage Stamps	V
A.2 List of GRG	XI
A.3 Python Code	XIII
A.3.1 Identifying GRGs	XIII
A.3.2 Plotting the postage stamps	XIV

List of Figures

1	The SEDs of star-forming galaxies and AGN.	3
2	Schematic drawings of the central engines of radiative-mode AGN and jet-mode AGN.	4
3	Components of a radiative-mode AGN.	5
4	A commonly used AGN unification model.	6
5	The line spectra of Seyfert 1s, Seyfert 2s, and LINERs.	8
6	Typical examples of FRI and FRII radio galaxies.	10
7	A size comparison chart of galaxies.	11
8	A size comparison chart of radio-loud AGN.	12
9	P-D Diagram showing the radio power-linear size relation as well as the evolutionary tracks of AGN.	14
10	Source association of radio data.	16
11	The WISE colour-colour diagram.	18
12	The redshift distribution of various source types.	19
13	The distribution of the 887.5 MHz luminosity against redshifts for various source types.	20
14	Postage stamps of two radio galaxies with seemingly FR II morphologies.	21
15	A zoomed-out view of a GRG postage stamp, revealing a larger structure.	22
16	Postage stamps of GRGs with ambiguous morphologies.	23
17	The angular size and physical size distributions of GRGs and WISE AGN.	24
18	The K-band magnitude distribution.	26
19	The optical g-r band magnitude distributions of GRGs and WISE AGN.	27
20	The distribution of star formation rates as a function of their stellar mass for GRGs and WISE AGN.	28
21	Postage Stamps of GRGs (1-12)	V
22	Postage Stamps of GRGs (13-24)	VI
23	Postage Stamps of GRGs (25-36)	VII
24	Postage Stamps of GRGs (37-48)	VIII
25	Postage Stamps of GRGs (49-60)	IX
26	Postage Stamps of GRGs (61-63)	X

List of Tables

1	The categorisation of AGN according to multiple shared properties	7
2	The counts and mean redshifts of different source types.	19
3	The mean K-band magnitudes of WISE AGN and GRGs.	26
4	Number of GRGs and WISE AGN with star formation rates and stellar masses.	28
5	The mean star formation rate and stellar mass values.	29
6	The K-S Test results for star formation rate and stellar mass.	29
7	List of all GRGs with important parameters.	XII

1 Introduction

Galaxies are celestial bodies that have piqued the interest of astronomers for centuries, with the first classification of these objects by French astronomer Charles Messier dating back to the 17th century. At the time, he merely classified these objects as a method of differentiating them from comets as he was an avid comet hunter, but little did he know the true nature of these objects. In total, 110 objects are contained within the Messier Catalogue and among them, 40 are classified as galaxies ([Messier & Niles, 1981](#)).

Setting Messier and his comet obsession aside, a few centuries later and the total number of galaxies in the universe is estimated to be around 200 billion (2×10^{11}) according to recent data obtained from NASA's New Horizons space probe ([Lauer et al., 2021](#)). Although this number is far fewer than initially estimated (~ 2 trillion), it is still difficult to comprehend such a scale. Constant research is being conducted to study these objects, with new discoveries changing the way we see and understand them. For example, a very recent study by [Ferreira et al. \(2022\)](#), based on data obtained from the James Webb Space Telescope (JWST; [Gardner et al. 2006](#)) indicates that at redshifts $z > 1.5$, galaxies show a higher percentage of disk morphologies (~ 10 times higher) compared to previous data obtained from the Hubble Telescope.

There exists a subgroup of galaxies that is particularly interesting called active galaxies. These galaxies host active galactic nuclei (AGN) that produce incredible amounts of energy in multiple wavelengths. Among them exist giant radio galaxies (GRGs), which are enormous and display spectacular jets in radio wavelengths, protruding up to megaparsec scales from their central regions. Their very nature is still a mystery to astronomers as these objects are sparse when compared to the vast quantity of discovered active galaxies. Investigating the complex mechanism in their central engines that produces these jets as well as their external properties (i.e. host galaxies and environments) can give us some very useful insight into how AGN activity affects galaxy evolution.

This thesis aims to study these fascinating objects in a particular field in the sky, where we have excellent radio and multi-wavelength data available. In Section 2, I provide information about AGN, their structures, properties and different classifications of AGN. In Section 3, I elaborate on the data used for this thesis and in Section 4, the analysis of the data is presented. The goal of this thesis is to investigate GRGs in the GAMA23 field and compare their properties (such as stellar mass, luminosity, star formation rate, etc.) with typical-size AGN to gain insight into the nature of GRGs. Throughout this thesis, I use the FlatLambdaCDM cosmology, with $H_0 = 67.7 \text{ km s}^{-1} \text{ Mpc}^{-1}$, $\Omega_m = 0.307$ for calculations.

2 Active Galactic Nuclei

An active galactic nucleus (AGN) is defined as a compact region at the center of massive galaxies ($M_\star \sim 10^7 M_\odot$), which are the most luminous sources of electromagnetic radiation in the universe. This radiation, which can be observed across the entire electromagnetic spectrum, is not due to the thermonuclear process from stellar activity but is instead caused by the accretion of matter onto the supermassive black hole (SMBH) at the center of the galaxy as well as emission from other components of the AGN structure, such as the dusty torus, radio jets, etc. The structure of AGN is further discussed in Section 2.2.

2.1 History of AGN discovery

The discovery of AGN can be traced back to the early 20th century, with the detection of strong emission lines in the nebula NGC 1068 by E.A. Fath at Lick Observatory (Peterson, 1997). However, it was Carl Seyfert (Seyfert, 1943) who first realised that several galaxies display similar optical spectra which were dominated by high-excitation nuclear emission lines and thus belonged in a class of their own. The prominent characteristics of these spectra were (i) broad lines (up to 8500 km s^{-1} , full width at zero intensity) and (ii) broader hydrogen lines than other lines. These galaxies are now known as Seyfert galaxies. However, they were not further studied until 1955, when they were also detected to be radio sources. The first attempt to understand the physics of these Seyfert galaxies was conducted by Lodewijk Woltjer (Woltjer, 1959) and resulted in the following findings:

1. The size of the nucleus has to be lesser than 100 pc because they are unresolved.
2. 1% of spiral galaxies discovered were found to be Seyfert galaxies. This lead to the conclusion that nuclear emission lasts for at least 10^8 years. The basis for this argument is that there are two possibilities: (i) Seyfert galaxies are always Seyferts, in the sense that their lifetime is the age of the universe ($\sim 10^{10}$ years); (ii) spiral galaxies undergo a Seyfert phase. Taking 1% of the age of the universe gives us $\sim 10^8$ years.
3. The mass of the nucleus must be very high if the material in that region is gravitationally bound. This argument stems from the velocity dispersion obtained from the widths of the emission lines, which were found to be of the order of 10^3 km s^{-1} .

These findings lead to some initial conclusions about AGN. Firstly, the sizes of these AGN are very small from an astronomical standpoint, however, they contain up to 10% of the mass of the galaxy. What is even more extraordinary is the high efficiency of the accretion of matter onto the SMBH. According to Kerr (1963) and Shapiro & Teukolsky (1983), this efficiency ranges from 5-42%, therefore enabling luminous AGN to be detected at high redshifts (i.e. for AGN at $2.0 < z < 2.5$: $L_x \sim 10^{43} \text{ ergs}^{-1}$; Aird et al. 2010).

2.2 AGN Structure

The spectral energy distribution (SED) of a galaxy shows the energy emitted by the galaxy as a function of either the wavelength or the frequency. Figure 1 illustrates the difference between the SED of a normal galaxy and an active galaxy. The most significant difference between the two galaxy types is the range of the SED curves. AGN show additional radio and X-ray emissions as well as a peak in the optical-ultraviolet (UV) region (i.e. the big blue bump, [Shang et al. 2005](#)), which are the results of the accretion of matter from the accretion disk onto the SMBH.

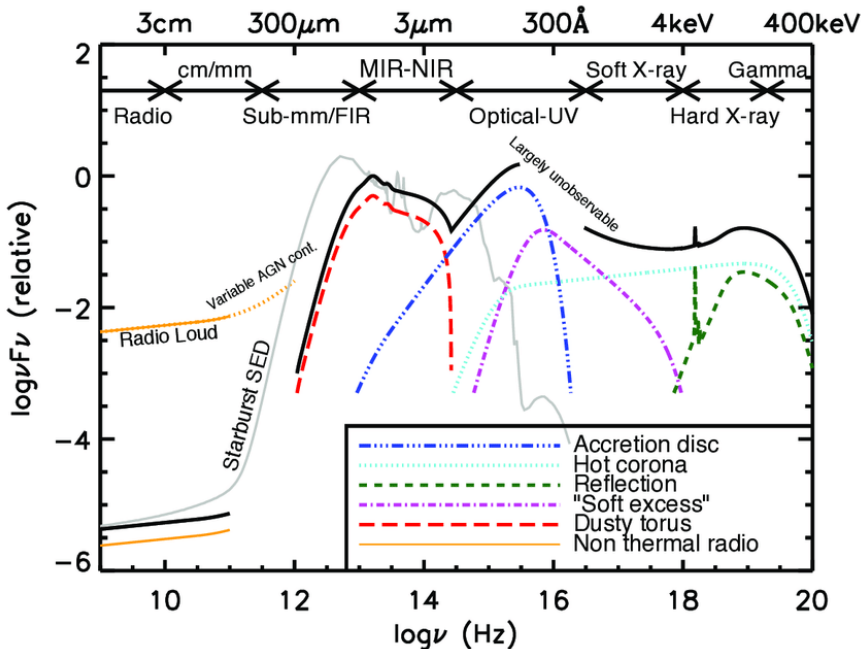


Figure 1: Comparison of the SEDs of a star-forming galaxy (grey curve) and an unobscured AGN (black curve), separated into the main physical components (colored curves; [Harrison 2014](#)).

It is important to note that there are two different modes of accretion with two different dominant energetic outputs, i.e. the radiative-mode and the jet-mode. The energy output of the radiative-mode is dominated by the efficient conversion of the potential energy into electromagnetic radiation caused by the accretion of matter onto the SMBH and this process is more commonly observed in Seyfert galaxies and quasars. The jet-mode on the other hand produces relatively low amounts of radiation. Instead, the energy output primarily consists of the transport of high amounts of kinetic energy through two-sided collimated jets, which can be observed in Low Excitation Radio Galaxies (LERGs). Figure 2 illustrates the difference between the two modes of AGN accretion.

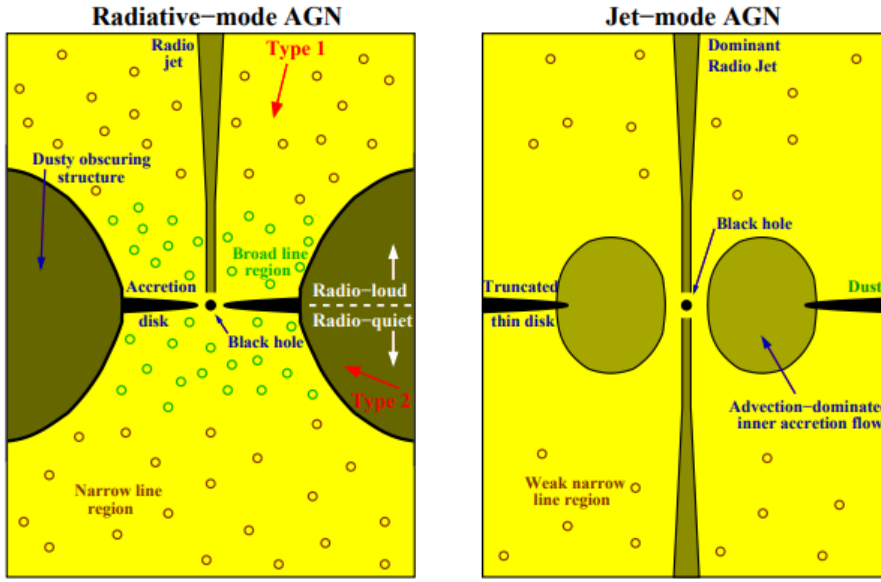


Figure 2: Schematic drawings of the central engines of radiative-mode and jet-mode AGN by Heckman & Best (2014).

For radiative-mode AGN, the SMBH is surrounded by a geometrically-thin, optically-thick accretion disk, from which the thermal continuum emission due to the accretion is observable in the visible and UV wavelengths. Surrounding this accretion disk, a hot electron plasma, known as the corona scatters the photons from the disk into the X-ray regime through Compton scattering. When these X-rays impact the accretion disk, they are absorbed and reflected by hot, dense, high-velocity gas clouds located within $\sim 1\text{pc}$ from the SMBH, producing electromagnetic emission in the visible, UV and near-infrared (IR) regime. This region is known as the Broad Line Region (BLR).

At larger scales, there exists a dusty toroidal structure (i.e. torus) made of hot molecular gas and dust that absorbs the UV and visible photons from the accretion disk as well as the soft X-rays from the corona. This process is known as extinction and results in thermal re-radiation in the IR regime. The column density of this obscuring torus has a range of 10^{23} to 10^{25} cm^{-2} . At the highest column densities where the medium is considered to be ‘Compton Thick’, even the hard X-rays from the corona are absorbed. At lower column densities, ionising radiation escapes along the polar axis of the torus, emitting forbidden emission lines in UV, optical and IR regimes by photo-ionising the surrounding gas. This region is known as the Narrow Line Region (NLR). The differences between these broad and narrow lines are further discussed in Section 2.3.

Figure 3 illustrates the multiple different components of a radiative-mode AGN, as well as some observational consequences that will be discussed further in Section 2.3.1.

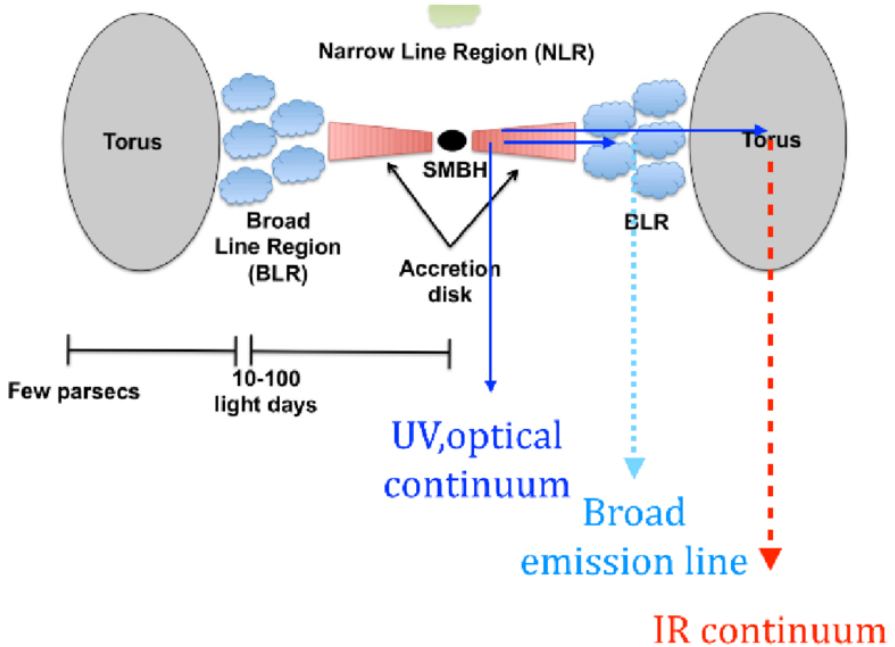


Figure 3: Components of a radiative-mode AGN by Doré et al. (2016).

For jet-mode AGN, the geometrically thin disk is absent and is replaced by a geometrically thick structure (Figure 2), in which the inflow time is much lower than the radiative cooling time. This is referred to as advection-dominated or radiatively inefficient accretion flows (ADAFs/RIAFs; Heckman & Best 2014), which are characterised as being able to launch two-sided jets. Due to synchrotron emission, these jets are easily detectable at radio wavelengths and can extend up to megaparsec scales in extreme cases. This mode is mostly observed in radio galaxies as well as its giant variant.

2.3 Unification models and AGN Taxonomy

2.3.1 Unification Models

There are many unification models proposed over the years to group AGN based on some shared properties. Peterson (1997) suggests that the goal of these unification models is to minimise the observed parameters required to explain the physical effects displayed by these AGN. Figure 4 illustrates a popular model by Heckman & Best (2014), which classifies AGN based on their radio-loudness, their orientation towards the observer, as well as their morphology.

The general consensus is that Type 1 and Type 2 AGN are the same objects, only viewed at different angles. When viewing a radiative-mode AGN at an angle which exposes the central engine, it is called a Type 1 AGN and we are able to observe the NLR as well as the BLR. Viewing it at steeper angles, however, prevents us from observing the BLR as the torus now blocks our view. These AGN are known as Type 2 AGN. This orientation-based classification applies to both radio-quiet AGN and radio-loud AGN. (i.e. for radio-quiet AGN: Seyfert 1s and 2s; for radio-loud AGN: broad-line radio galaxies [BLRG] and

narrow-line radio galaxies [NLRG]).

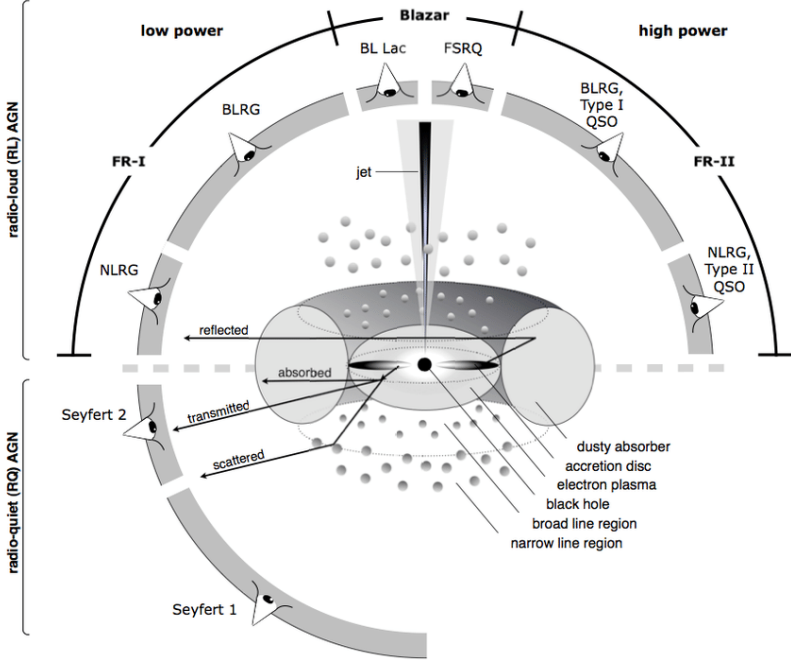


Figure 4: A commonly used AGN unification model by Heckman & Best (2014).

In reference to radio loudness, AGN can generally be stated to have a strong dichotomy between radio-loud or radio-quiet classes ([Dermer & Giebels, 2016](#)). An important distinction between the two is the existence of jets and lobes in radio-loud AGN, which dominate the radio emission from these objects. This is rather convenient for identifying and classifying various objects. However, this is also a rather archaic distinction. Traditionally the ratio of radio flux density to optical flux density has been used to classify radio sources as being either radio-quiet or radio-loud, however, this convention was somewhat arbitrary. [Gürkan et al. \(2019\)](#) investigated the largest quasar sample using high-resolution and sensitive radio data to show that there is no clear dichotomy but instead quasars (i.e. radiatively efficient accretion systems) show a wide continuum of radio properties.

In addition to that, Figure 4 also shows that radio-loud AGN can be split into two groups, i.e. ‘low power’ and ‘high power’. This directly corresponds to the different accretion modes as explained in Section 2.2. It is important to note that these unification models do not classify AGN with a 100% accuracy. For example, the existence of “true” Seyfert 2 galaxies ([Bianchi et al., 2012](#)) indicate that there are exceptions to these models and further research has to be conducted to improve our ability to construct more accurate models. Therefore, until a perfect unification model is achieved, categorising AGN as shown in Table 1 presents us with a clear and easy-to-understand method to identify various AGN subtypes based on their shared properties.

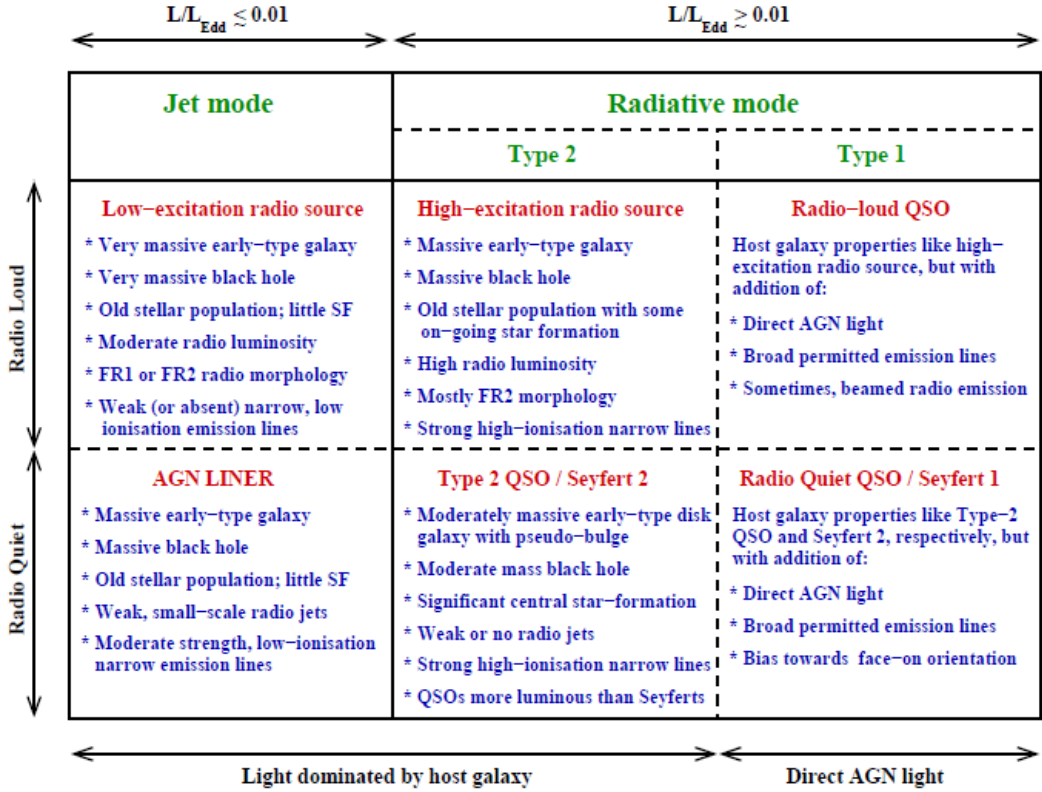


Table 1: The categorisation of AGN according to multiple shared properties by [Heckman & Best \(2014\)](#).

2.3.2 Seyfert galaxies

As stated in Section 2.1, Seyfert galaxies were initially discovered in the early 20th century. Seyfert galaxies are radio-quiet AGN, which exhibit a lower optical luminosity of $M_B > -21.5$, according to [Schmidt & Green \(1983\)](#), who used this luminosity criterion to distinguish Seyfert galaxies from quasars. This by no means indicates that Seyfert galaxies are not bright. On the contrary, Seyfert galaxies tend to look like regular spiral galaxies with a star superimposed on the center, whereas the nuclei of quasars even outshine their host galaxy.

Seyfert galaxies can be divided into Type 1 Seyfert galaxies (Seyfert 1s) and Type 2 Seyfert galaxies (Seyfert 2s). This classification, made by [Khachikian & Weedman \(1974\)](#), is based on observational differences, specifically the existence of broad permitted lines and narrow forbidden lines. The spectra of Seyfert 1s consist of two sets of emission lines superimposed on each other. One set of these lines exhibit characteristics of low density (electron density $n_e \sim 10^3 - 10^6 \text{ cm}^{-3}$) ionized gas with a Full Width at Half Maximum (FWHM) corresponding to several hundred km s^{-1} . These lines are referred to as ‘narrow lines’ and it is important to note that these lines are wider than emission lines in non AGNs. The other set of lines are the ‘broad lines’, which can have a FWHM of up to several thousand km s^{-1} . An interesting feature of these permitted lines is that they indicate that the broad-line gas is of high density (electron density $n_e \geq 10^9 \text{ cm}^{-3}$).

Figure 5 shows different spectral lines for different types of AGN, where the top image shows the spectra of the Seyfert 1 galaxy NGC 5548, the top part of the bottom image shows the spectra of the Seyfert 2 galaxy NGC 1667, and the bottom part of the bottom image shows the spectra of the LINER (see Section 2.3.3) NGC 1052. The broad lines (e.g. Balmer lines [$\text{H}\alpha$, $\text{H}\beta$, etc.], He I, He II) are seen in Seyfert 1s but are either completely missing or barely visible for Seyfert 2s, while the narrow lines (e.g. [OII], [OIII], [NII]) are observable in both spectra.

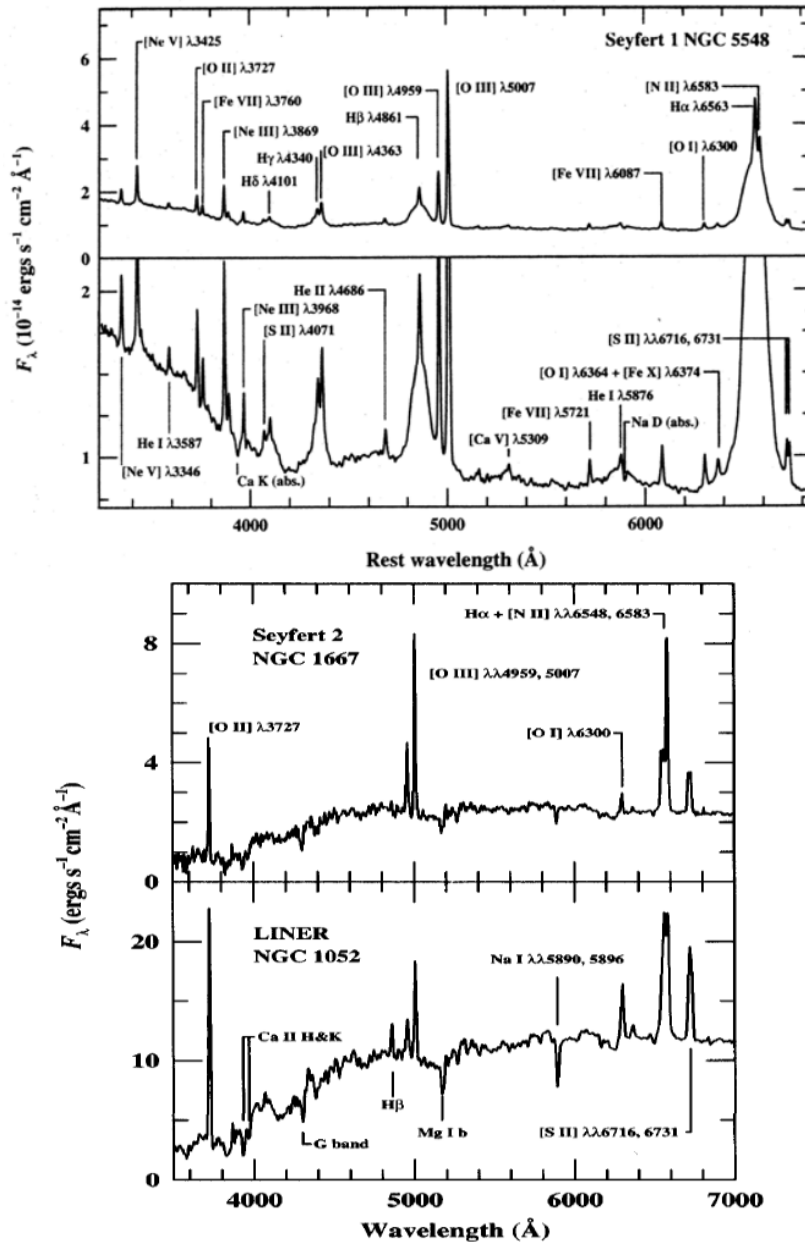


Figure 5: Top-panel: Line spectra of a Seyfert 1 galaxy NGC 5548; Bottom-panel: Line spectra of a Seyfert 2 galaxy NGC 1667 and LINER 1052 (Peterson, 1997).

2.3.3 LINERs

Low ionisation nuclear emission-line regions (LINERs) are another class of optically classified AGN that spectroscopically resemble Seyfert 2 AGN, except that the low-ionisation lines, e.g. [OI] and [NII] are relatively strong. [Ho et al. \(1997\)](#) suggest that LINERs are very common, and might be present at detectable levels in nearly half of all spiral galaxies. Figure 5 also shows that LINERs can be distinguished from Seyfert galaxies using the strength of their optical emission lines (e.g. [Baldwin et al., 1981](#)).

2.3.4 Quasars

Quasars are considered to be the most luminous subclass of AGN, with nuclear magnitudes $M_B < -21.5$. Unlike Seyfert galaxies, the host galaxies of quasars are usually out-shined by their central region. Therefore, they tend to look like compact bright sources, with angular sizes smaller than ~ 7 arcsec ([Peterson, 1997](#)) and many of these sources are surrounded by a low surface brightness halo (also known as the ‘quasar fuzz’) which does seem to be light from the host galaxy. Some quasars even have unique features, such as optical jets. Quasars can be divided into radio-loud quasars and radio-quiet quasars. The former is commonly referred to just as quasars, while the latter is commonly referred to as quasi-stellar objects (QSO) and are the more common type of quasars (about 90%). This distinction however is nowadays interchangeable in literature. Similarly to Seyfert galaxies, radio-quiet quasars can also be classified according to their spectral lines into Type 1 and Type 2 quasars, using criteria stated in Section 2.3.1.

Quasars are not only some of the most luminous objects in the universe, but they are also some of the furthest objects that we can observe. This indicates that quasars are more common in the early universe, and as the SMBH eventually consumes all the matter around it, the energy production of the quasar eventually comes to an end. Various studies (e.g. [Matteo et al., 2005](#)) suggest that the Milky Way and other galaxies would have possibly gone through an active stage in the past and that their SMBH are now dormant due to a lack of accretion matter.

2.3.5 Blazars

Blazars are extremely luminous radio-loud AGN that show abnormally large short time-scale variations in multiple wavelengths (i.e. up to 50% on time scales as short as one day) and high amounts of polarization. These properties tend to stem from the fact that the jets of blazars are oriented close to our line of sight.

Blazars can be classified into two groups: ‘optically violent variables (OVV) quasars’ or ‘BL Lac objects’. OVVs are radio-loud quasars that show strong variability and polarization in their radio and optical emission. BL Lacs on the other hand are thought to be similar to low-power radio galaxies with radio jets oriented close to our line of sight. A study by [Falomo et al. \(2014\)](#) shows that the spectra of BL Lac objects exhibit non-thermal continuum emission over the whole electromagnetic range. The absence of stronger emission and absorption lines relative to this continuum emission makes studying their nature and determining their redshifts very difficult.

2.3.6 Radio galaxies

Radio galaxies are mostly large elliptical galaxies with a radio-loud AGN that produce radio jets and radio lobes which extend well beyond the visible host galaxy ([Jones et al., 2004](#)). The emission of these jets and lobes is due to the non-thermal synchrotron radiation caused by the acceleration of relativistic electrons in a magnetic field. The length of these jets and lobes reaches up to a few megaparsecs and their radio luminosities can reach values up to 10^{39} W with a frequency range of 10 MHz to 100 GHz. Star formation also results in radio emissions, and is the dominant source of radio waves seen in normal galaxies. This emission is mainly due to (i) free-free emission from HII regions (thermal), which dominate the high radio frequencies; (ii) synchrotron radiation (non-thermal) from electrons accelerated by supernova remnants, which dominate the low radio frequencies (see [Condon, 1992](#)). For radio sources with unresolved structures (i.e. no visible jets or lobes), the radio emission observed can be dominated by either AGN activity or star formation or even both.

Radio galaxies can also be classified according to their large-scale radio morphology. In this regard, [Fanaroff & Riley \(1974\)](#) divided radio galaxies into two classes: Fanaroff and Riley Class I (FRI), and Class II (FRII). The distinction between the two classes comes from the distance between the brightest points in the radio emission, i.e. FRI sources were brighter in the centre, where the host galaxy resides, while FRII sources were brightest at the edges, forming lobes and hotspots. This difference in structure results in a difference in brightness between the two classes, i.e. FRIs having a lower luminosity than FRIIs, though this picture is changing with recent sensitive radio surveys (e.g. [Mingo et al., 2019](#)).

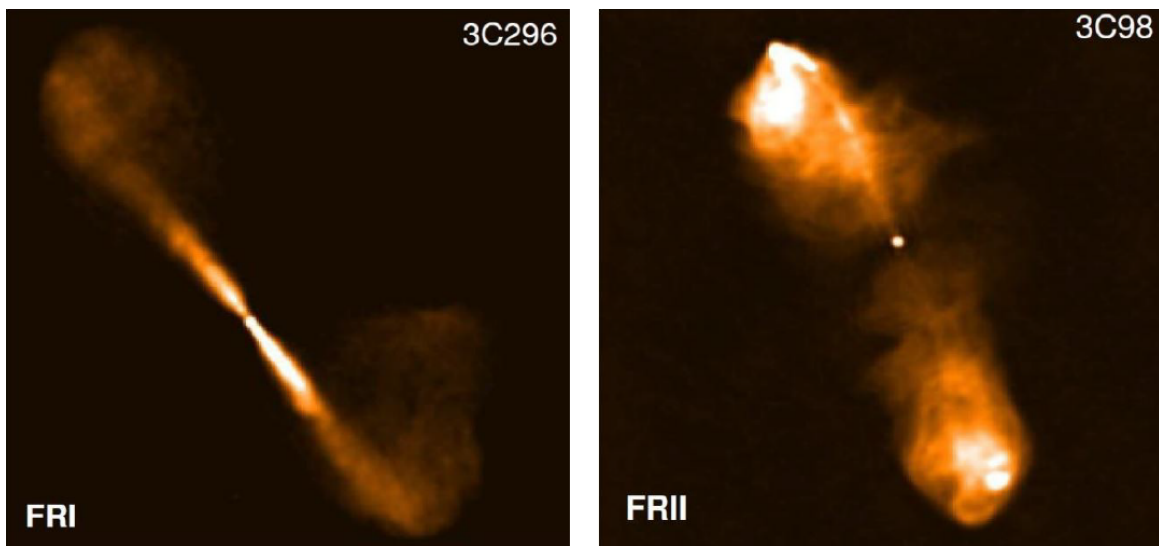


Figure 6: Typical examples of FRI and FRII radio galaxies ([Tadhunter, 2016](#)).

In addition to a morphological classification, radio galaxies can also be classified according to their optical spectroscopic properties into high-excitation radio galaxies (HERGs) and low-excitation radio galaxies (LERGs). [Laing et al. \(1994\)](#) classified HERGs as sources

which have the line flux ratio $[\text{OIII}]/\text{H}\alpha > 0.2$ and equivalent widths of $[\text{OIII}]5007 > 3\text{\AA}$. HERGs can be further classified into broad-line radio galaxies (BLRGs) and narrow-line radio galaxies (NLGRs) according to the line widths of their emission lines, as radio-loud analogues to Seyfert 1s and Seyfert 2s respectively. On the contrary, the optical spectra of LERGs show only absorption spectra similar to that of giant elliptical galaxies and very weak $[\text{OII}]3727$ emission lines (Hine & Longair, 1979). From the above classification criteria by Laing et al. (1994), LERGs inversely show a line flux ratio $[\text{OIII}]/\text{H}\alpha < 0.2$, as their $[\text{OIII}]5007$ emission is relatively weaker than HERGs or sometimes even undetectable. An important fact to note is that while the majority of HERGs have FR II morphologies, recent radio surveys show that more HERGs with FR I morphologies are being discovered (e.g. Gürkan et al., 2021). On the other hand, there are already large samples of LERGs showing both FR I and FR II morphologies (Mingo et al., 2019).

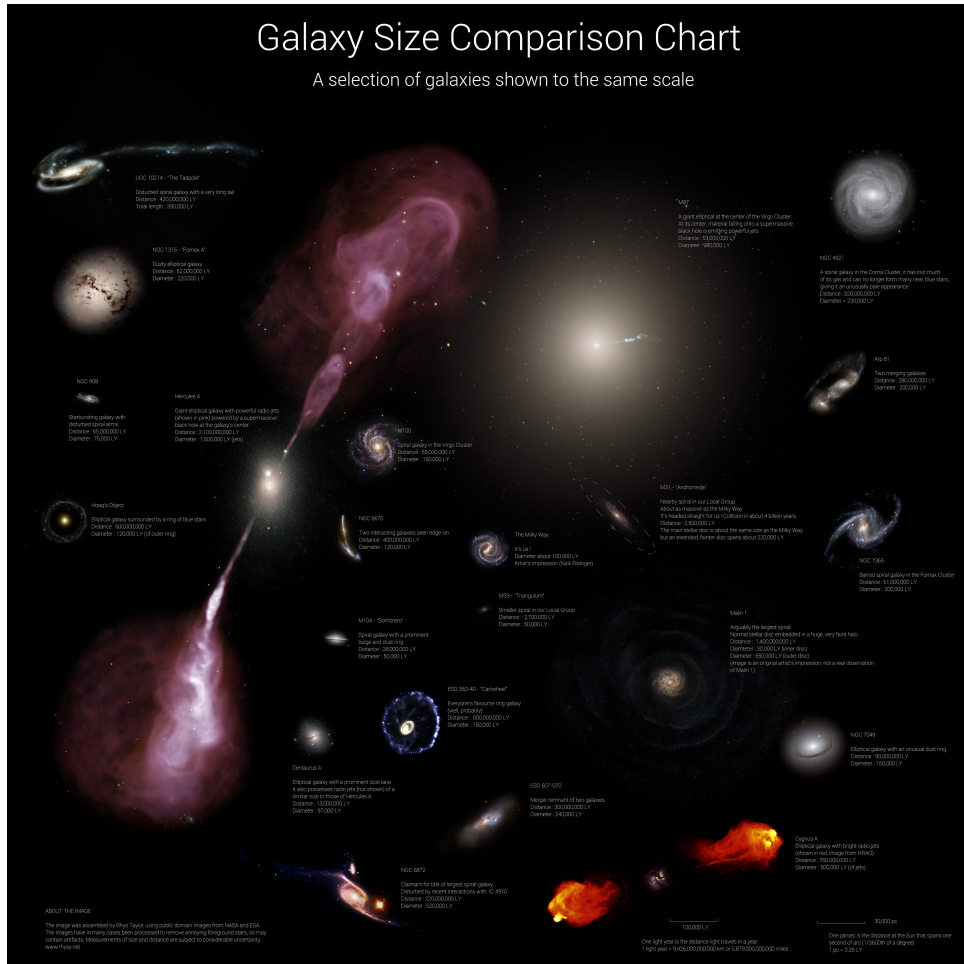


Figure 7: A size comparison chart of galaxies by Rhys Taylor. The host galaxy of the GRG, Hercules A, displays a similar size to other galaxies seen in the image. Its radio jets (pink), however, reach incredible distances.

In order to understand the actual scale of these radio jets, Figure 7 by Rhys Taylor ¹

¹<http://www.rhysy.net/galaxy-sizes.html>

shows a size comparison of a wide range of galaxies. Among them, one galaxy stands out: Hercules A, a.k.a. 3C 348. This bright radio source was discovered in the mid-20th century using the Cambridge Interferometer of the Cavendish Observatory at Cambridge University.

2.3.7 Giant Radio Galaxies

While Hercules A displays impressive jets which extend up to the length of several galaxies, it is nowhere near the largest discovered galaxies in the universe. That title belongs to giant radio sources (GRSs), which refers to giant radio galaxies (GRGs) and giant radio quasars (GRQs). These radio sources have extended jets that exceed the 0.7 Mpc threshold and the largest discovered source, Alcyoneus ([Oei et al., 2022](#)) has an astounding 4.98 Mpc linear size, as shown in Figure 8 by [Dabhade et al. \(2022\)](#), which compares some of the largest GRS with two very well known radio galaxies, Hercules A and Cygnus A (their jets can be seen in Figure 7).

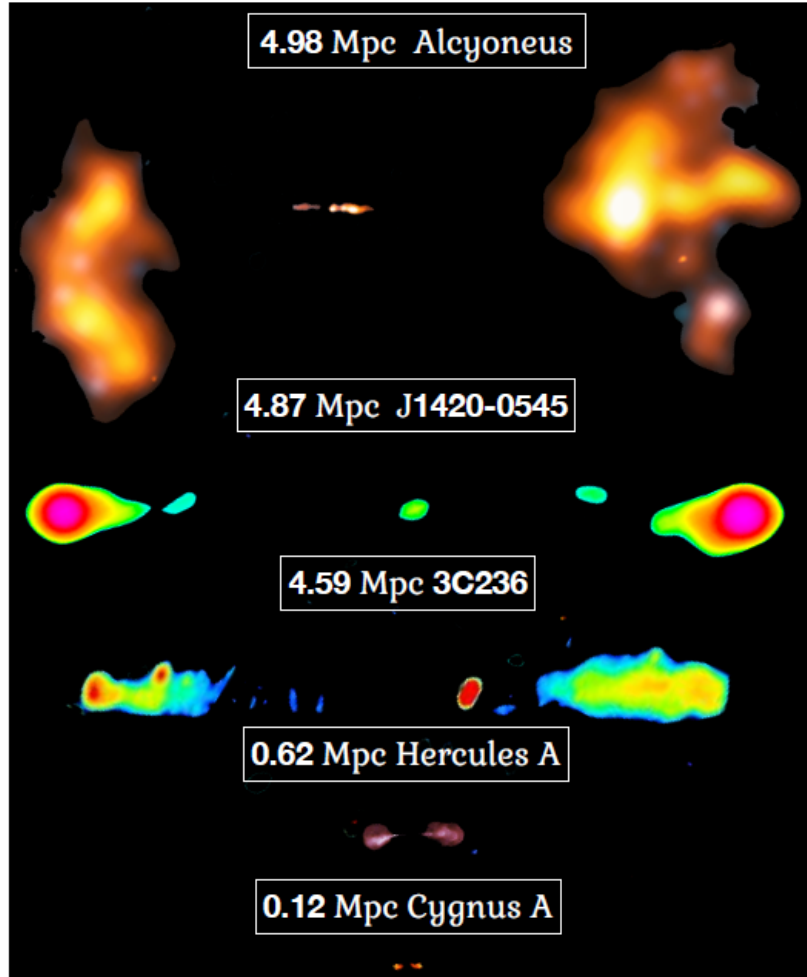


Figure 8: A size comparison chart of radio-loud AGN by [Dabhade et al. \(2022\)](#), showing some of the largest jetted structures discovered.

In terms of their position on the galactic evolutionary scale, GRSs are situated at the tail end. The jet power of these sources ranges from 10^{36} to 10^{39} W ([Dabhade et al., 2022](#)), which results in them reaching Mpc scales faster than low-power ones.

Figure 9 shows a radio power-linear size (P-D Diagram) by [Gürkan et al. \(2022\)](#) which demonstrates this relation. This diagram serves to illustrate the evolutionary path of radio-loud/jetted-AGN populations, and the crosses are in intervals of 50 Myr with the complete evolutionary track spanning a total of 500 Myr ([Hardcastle et al., 2019](#)). This diagram shows that jetted AGN with long lifespans spend most of their life as unresolved radio sources with sizes between a few tens and a few hundred kiloparsecs.

The Australian Square Kilometre Array Pathfinder (ASKAP) radio luminosities of sources at 887.5 MHz were extrapolated to 150 MHz using a spectral index of 0.7 in order to compare the AGN from this catalogue with other AGN catalogues.

Optical studies show that almost all GRSs have elliptical galaxies as hosts, similar to standard radio galaxies (SRGs). However, their stellar populations differ slightly, with GRGs having a more intermediate-age stellar population (9×10^8 yrs - 7.5×10^9 yrs) than SRGs according to one study by [Ku  nicz et al. \(2019\)](#).

Major radio surveys conducted at low radio frequencies (i.e. Low Frequency Array Two-metre Sky Survey-LoTSS at 144 MHz; [Shimwell et al. 2022](#)) to ones at high frequencies (i.e. the National Radio Astronomy Observatory Very Large Array Sky Survey-NVSS at 1400 MHz; [Condon et al. 1998](#)) were compiled and tabulated to determine the total number of GRSs discovered ([Dabhade et al., 2022](#)). Across a total of 22 surveys conducted over several decades, only ~ 2300 GRSs have been identified according to the current cosmological model. This number pales in comparison to the total number of active galaxies in the observable universe. It is important to note that this number only represents the number of GRSs that have corresponding host galaxies and redshifts. Better optical and spectroscopic studies are required to identify GRSs more accurately.

Many astronomers have suggested possible explanations for the sparseness of GRSs: (i) GRSs thrive in low-density environments, allowing their jets to reach incredible sizes ([Mack et al., 1998](#), [Malarecki et al., 2015](#)); (ii) the central engines of GRSs are stronger than typical-size AGN (see [Gopal-Krishna et al., 1989](#)), allowing them to produce immensely powerful jets ([Wiita et al., 1989](#)); (iii) GRSs sometimes display discontinuous jets, suggesting that the AGN activity occurs recurrently ([Subrahmanyam et al., 1996](#)). These possibilities are unfortunately not solid enough to explain the existence of GRSs on their own as there are many exceptions, and it is likely that it depends on the combination of these factors as well as other phenomena which have not been documented yet. For a comprehensive review of giant radio galaxies, please refer to [Dabhade et al. \(2022\)](#).

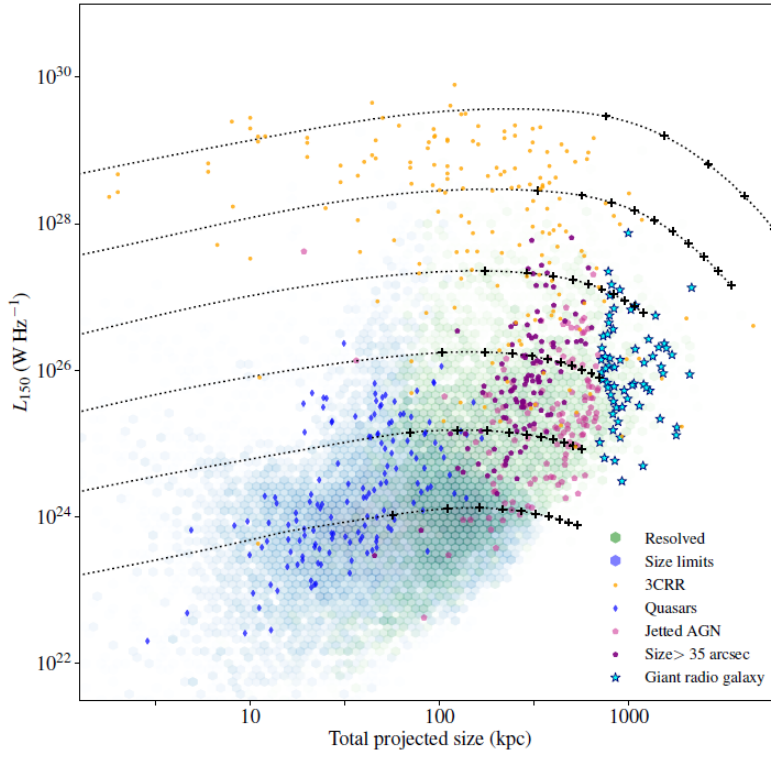


Figure 9: P-D Diagram showing the radio power-linear size relation as well as the evolutionary tracks of AGN (see [Gürkan et al., 2022](#)). The crosses are in intervals of 50 Myr with the complete evolutionary track spanning a total of 500 Myr ([Hardcastle et al., 2019](#)). The ASKAP radio luminosities of sources at 887.5 MHz were extrapolated to 150 MHz using a spectral index of 0.7 in order to compare the AGN from this catalogue with other AGN catalogues.

3 Data

3.1 Radio Data

This thesis is based on the radio observations of the GAMA23 field as part of the Galaxy And Mass Assembly (GAMA) survey ([Driver et al., 2011](#)). This field is a $\sim 50 \text{ deg}^2$ field with a Right Ascension (RA) centered around 23h and covers a Declination (DEC) range of -35° to -30° . The radio observations of the GAMA23 field were carried out using the Australian Square Kilometer Array Pathfinder (ASKAP) at 887.5 MHz, covering a wide 82.7 deg^2 field as part of the Evolutionary Map of the Universe ([Norris et al., 2011](#)). In order to cover the full 50 deg^2 GAMA23 field, two ASKAP tiles were used. The data were processed using the latest version of ASKAPSoft pipeline and mosaicing tools were used to combine the two tile images to cover a wider (82.7 deg^2) area with a high resolution of 10 arcsec and a high central root-mean-square (rms) value of $38 \mu\text{Jy beam}^{-1}$.

Using the Python Blob Detector and Source Finder (PyBDSF; [Mohan & Rafferty 2015](#)), a total of 54814 radio sources were extracted, with 40186 objects having a peak flux threshold of 5σ (Peak flux density/ Island rms ≥ 5.0). The accuracy of this flux scale was evaluated by comparing this catalogue with various different radio catalogues that cover the GAMA23 field such as the Sydney University Molonglo Sky Survey (SUMSS; [Mauch et al. 2003](#)), the NRAO VLA Sky Survey (NVSS; [Condon et al. 1998](#)), TIFR Giant Metrewave Radio Telescope (GMRT) Sky Survey (TGSS; [Intema et al. 2017](#)), GaLactic and Extragalactic All-sky MWA survey (GLEAM; [Hurley-Walker et al. 2016](#)), and Rapid ASKAP Continuum Survey (RACS; [Hale et al. 2021](#)). This detailed analysis of the radio data showed that the survey has a correct flux scale ([Gürkan et al., 2022](#)). The astrometric precision was then evaluated and corrected using further GAMA source products, as seen in Section 3.2.

In order to reliably identify AGN from these radio sources, the source catalogue was thoroughly processed. Artefacts were identified and consequently removed, and source association, as well as optical identification processes, were conducted. A visual inspection was further carried out utilising radio and multi-wavelength data, which is discussed in Section 3.2, to accurately associate multiple radio components that belong to the same source and obtain the right host galaxy counterparts (see Figure 10). Finally, the total number of radio sources obtained after the processes is 39812 (i.e. where the multi-component radio sources were identified and stored as single sources with correct flux densities and sizes). For the analysis part of this thesis, I used the final value-added radio catalogue along with the final mosaic provided by [Gürkan et al. \(2022\)](#).

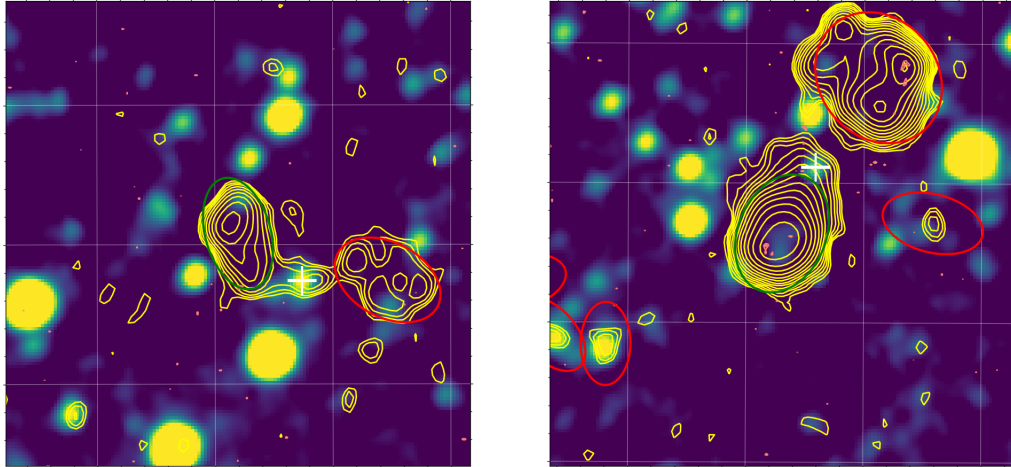


Figure 10: Source association on example postage stamps by [Gürkan et al. \(2022\)](#).

3.2 Multi-wavelength Data

The multi-wavelength catalogue used to identify and associate host galaxies to the radio sources consists of data sets that are part of the GAMA collaboration ([Driver et al., 2011](#)), namely the photometric catalogue KidsVikingGAMAV01 ([Bellstedt et al., 2020](#)), the spectroscopic redshift catalogue SpecObjv27 ([Liske et al., 2015](#)), and the spectroscopic line measurements from the GaussFitSimplev05 and GaussFitComplexv05 catalogues ([Gordon et al., 2016](#)). The following multi-wavelength data sets are contained within the GAMA catalogues:

- Ultraviolet: GALEX-FUV and NUV.
- Optical: VST KiDS u, g, r, i .
- Near- and Mid-Infrared: AllWISE W1,W2,W3,W4, at 3.4, 4.6, 12 and 22 μm respectively.
- Far-Infrared: Herschel SPIRE 250, 350, 500 μm .

This catalogue is rather comprehensive since it produces spectroscopic information with a 95% completeness with the VST KiDS i magnitude of 19.2 ([Liske et al., 2015](#)). [Gürkan et al. \(2022\)](#) also used classification methods described by [Bourne et al. \(2016\)](#) and [Baldry et al. \(2012\)](#) to eliminate radio sources with host galaxies that are flagged as stars. Furthermore, two photometric redshift catalogues: a photometric redshift (photo-z) catalogue from the HELP collaboration ([Shirley et al., 2021](#)) and the catalogue gkvEAZYPhotozv02 from the GAMA DR4 data product were used. Additional catalogues containing redshift values, such as the KiDS DR4 quasar catalogue and the KiDS DR4 bright galaxy catalogue, were also considered. However, cross-matching the redshifts of the sources from these catalogues yielded no additional results, therefore they were omitted from the finalized catalogue.

The priority of redshift values used is as follows:

1. spectroscopic redshift ‘Z_tilv11’ with ‘NQ_tilv11’ > 2
2. photometric redshift ‘redshift_h’
3. photometric redshift ‘z_peak’ with ‘science_primary’ = True

These multi-wavelength data were also utilized to extract information about the physical properties of our sources. For example, Code Investigating GALaxy Emission (CIGALE; Boquien et al., 2019) was utilized to obtain the star formation rate, stellar mass and dust luminosity by comparing the observed SEDs of galaxies with modelled ones. Gürkan et al. (2015) investigated far-IR properties of different galaxy populations (star-forming galaxies, composites and AGN) and estimated their mean dust temperatures using far-IR data from Herschel. They also explored the relation between star formation rate (derived using SED fitting) and far-IR luminosity at 250- μ m for star-forming objects. In the catalogue used for this thesis, there are also star formation rates available for AGN with far-IR flux densities at 250- μ m, which are estimated using the relation mentioned above and the mean dust temperature published by (Gürkan et al., 2015). Non-thermal AGN radiation can contaminate the far-IR emission (e.g. Kalfountzou et al., 2014), therefore the star formation rates derived using Herschel 250- μ m fluxes were assessed for possible AGN contamination and it has been found not to be a major effect. Where available I use star formation rates provided by the HELP collaboration for the samples investigated in this thesis, otherwise I use star formation rates derived using the relation above.

4 Analysis and discussion

4.1 Sample Selection

4.1.1 GRG selection

This thesis aims to investigate the properties of GRGs and as such, an essential condition must first be met in order to classify a radio source as a GRG, i.e. its radio jets must extend to a distance that is greater than 0.7 Mpc. The determination of this parameter was conducted in two steps. Firstly, [Gürkan et al. \(2022\)](#) calculated the ‘Angular size’ of the radio sources by taking the mean value of the largest convex hull around the set of elliptical Gaussians (‘Length’) and the distance between the separation of components (‘Separation’), as seen in Figure 10. Next, using reliable redshift values as explained in Section 3.2, I calculated the ‘Angular Diameter Distance’ of the sources using a Python script, utilising the astropy.cosmology package. These values were then multiplied with the ‘Angular Size’ obtained previously to determine the ‘Physical Size’ of the jets:

$$\text{Physical Size} = \text{Angular Size} \times \text{Angular Diameter Distance} \quad (1)$$

A total of **63** GRGs with reliable redshift values were then identified by considering only ‘Physical Size’ values greater than 0.7 Mpc.

4.1.2 Typical-size AGN selection

After obtaining the GRG sample, the identification of typical-size AGN (hereby known as WISE AGN) was conducted in order to compare their properties with GRGs. This selection was done using the AllWISE colours (refer to Section 3.2), by making a cut at $W1-W2 \geq 0.7$ for AGN (Figure 11), which is a reasonable colour cut (typical values between 0.5 and 0.8) that increases the size of the WISE AGN sample at the cost of reduced reliability (see [Stern et al., 2012](#)).

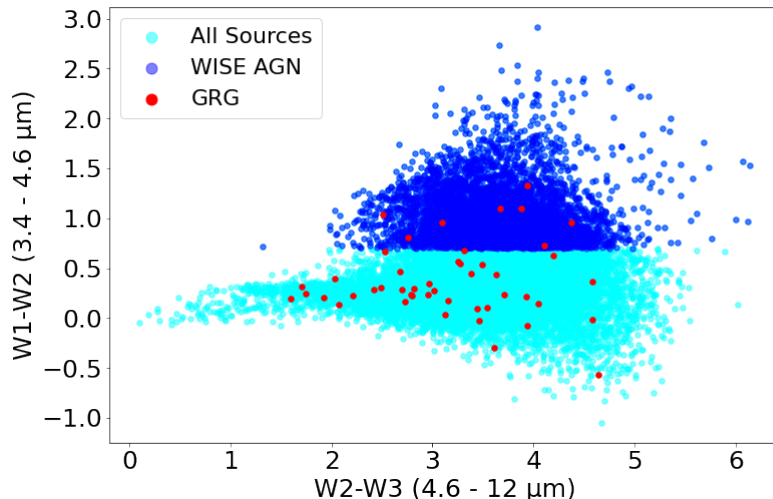


Figure 11: WISE colour-colour diagram used to select typical-size AGN.

From the 39812 objects, a total of 5217 objects ($\sim 13\%$) satisfy this condition. It is important to note that the GRGs obtained previously are excluded from this AGN sample. A further cut was made in order to identify AGN that have reliable redshift values ($z > 0$). This brings our total number of AGN down to 2964 ($\sim 7\%$ of the original sample). However, this additional condition is not an absolute necessity to determine the validity of the AGN as many AGN properties are not dependent on their redshift values, such as their K-band magnitudes, and angular sizes. Figure 12 shows the distribution of redshifts and Table 2 shows the counts and mean redshifts with their standard errors for the various radio sources.

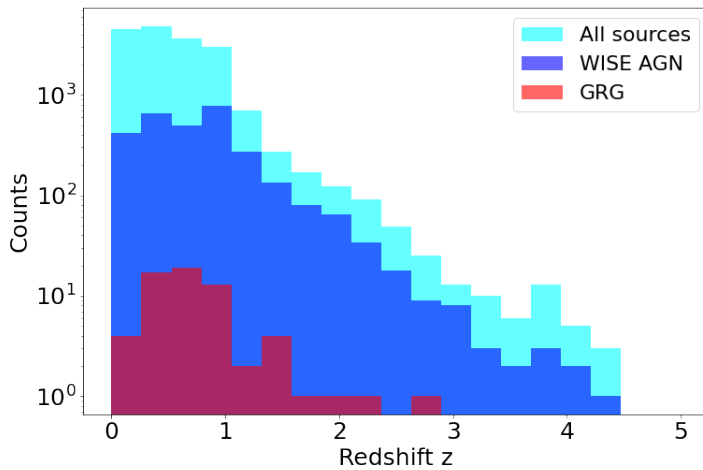


Figure 12: Redshift distribution of all radio sources, WISE AGN, and GRGs.

Source Type	Count	Mean Redshift
Total Sources in catalogue	39812	-
Sources with redshifts	17391	0.5722 ± 0.0032
Sources without redshifts	22421	-
WISE AGN with redshifts	2964	0.7896 ± 0.0097
WISE AGN without redshifts	2253	-
Giant radio galaxies	63	0.7547 ± 0.0592

Table 2: The counts and mean redshifts of different source types, with their standard errors.

Due to the varying sample sizes, the mean redshift values of all source types vary largely. Both GRGs and WISE AGN have mean redshifts larger than the overall mean redshift value, with $z_{WISE} > z_{GRG}$. The mean redshift for GRGs also shows a higher standard error than the other two samples due to its small sample size.

Using these redshift values, the 887.5 MHz radio luminosities of the sources were compared (see Figure 13). These radio luminosities were estimated using the measured flux densities and the equation given below:

$$L = 4\pi F D_L^2 \quad (2)$$

where F stands for the radio flux density, with a K-correction given by $(1+z)^{-(1+\alpha)}$, with spectral index $\alpha = -0.7$; and D_L stands for the Luminosity distance, which is calculated using the `astropy.cosmology` package which utilizes the redshift values of the sources.

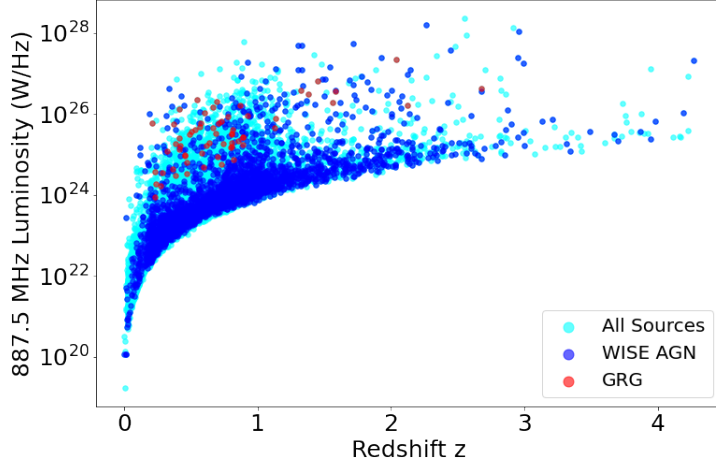


Figure 13: The distribution of the 887.5 MHz luminosity against redshifts for all sources, WISE AGN, and GRGs.

Figure 13 shows a general trend of increasing radio luminosities with increasing redshifts. In general, the GRGs show higher luminosity values than the WISE AGN. However, despite their sizes, their luminosities do not reach the highest end of the distribution. The implications of these observations will be further discussed in Section 4.3.

4.2 Evaluation of GRG sample

The initial evaluation of the GRG sample is conducted through a visual inspection of the radio data. I created postage stamps of all 63 sources by superimposing the contour lines from the G23 radio mosaic onto WISE images obtained from the [IRSA](#) data archive access tool. The contour lines show reliable radio emission at 3σ . Just by observing these images, many properties of the GRGs can be determined, such as their morphology, their orientation towards us, and in some cases, the conditions of their environments. In general, it is found that a large majority of these GRGs possess an FRII morphology, as the presence of large lobes at the end of the jets are abundantly clear. However, in some cases, the morphologies of the GRGs are uncertain as the radio data do not indicate a coherent structure, and in a few cases, the radio data indicate that the source is part of a galaxy cluster. These ambiguous cases are discussed in Section 4.2 and only their postage stamps are shown in this section, while the rest are added to the Appendix A.

4.2.1 Ambiguous cases

Galaxy clusters

Figure 14 shows two sources which are part of the galaxy cluster AC114 (see [Proust et al., 2015](#)). From the source association done by [Gürkan et al. \(2022\)](#), these sources appear to be GRGs with FR II morphologies based on the length of their jets and the brightness of their “lobes”, however taking a look at a larger region around the sources in Figure 15 indicate that they are part of a larger structure. It is still possible that the bright “lobes” are proof that these sources are FR II radio galaxies, however further evaluation of this galaxy cluster conducted at higher resolutions is necessary to adequately identify the nature of these sources.

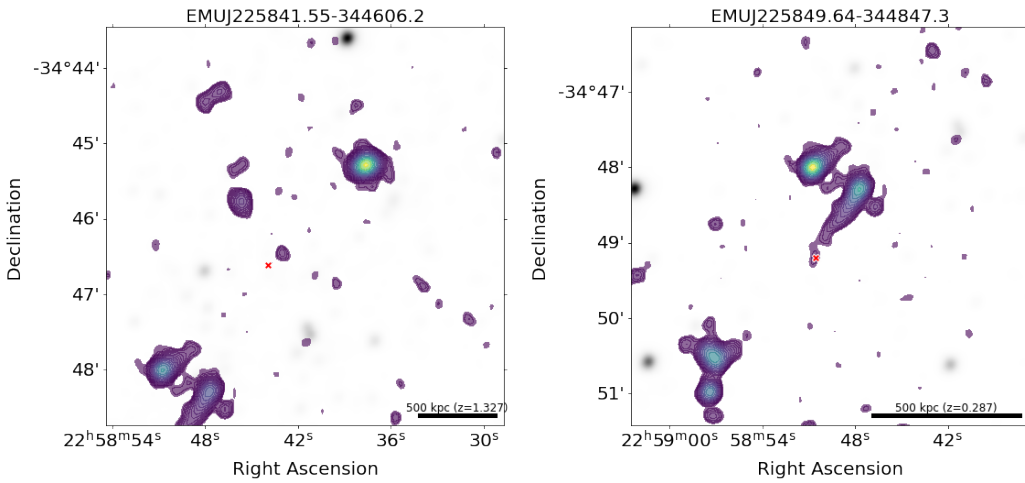


Figure 14: Two radio sources, EMUJ225841.55-344606.2 (left) and EMUJ225849.64-344847.3 (right) with seemingly FR II morphologies.

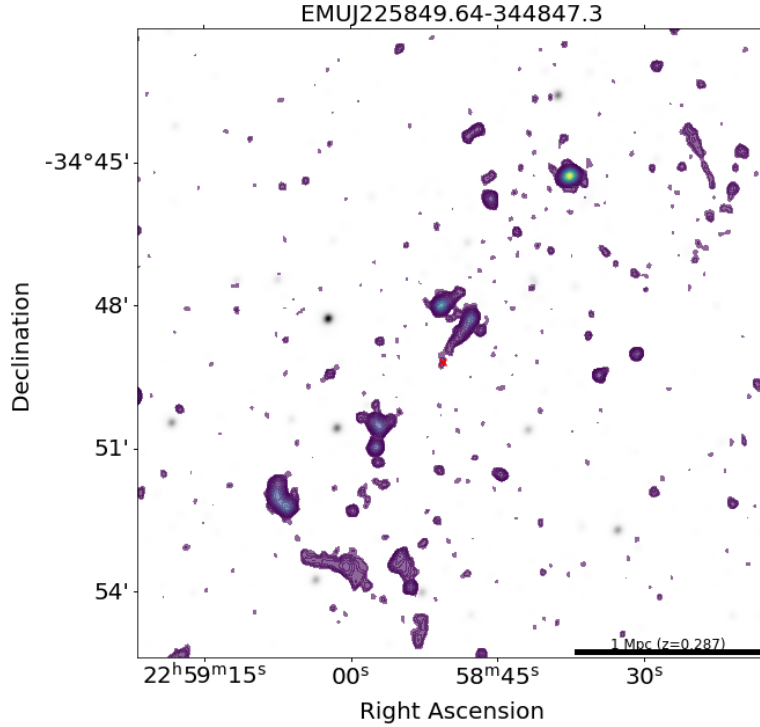


Figure 15: Radio source EMUJ225849.64-344847.3 viewed from a larger distance, revealing a large galaxy cluster, AC114.

Faint/Unique sources

The following sources exhibit either faint or rather unique radio emissions, making it challenging to identify their structure and nature. Higher resolution studies utilising more sensitive radio flux measurements are necessary to unravel more information about these sources. The postage stamps of the sources are shown in Figure 16.

The sources EMUJ224344.40-340128.6 (top left) and EMUJ231545.59-315421.3 (top right) display similar characteristics. They both seemingly have FR II morphologies, however, their jets are very faint. One possibility is that their central engines are currently in a dormant state, causing a lack of constant outflow and the lobes that can be seen in Figure 16 are the remnants of past AGN activity.

When considering how the jets of radio galaxies are formed, the existence of one-sided jets seems unconventional. However, sources EMUJ225854.18-345350.5 (middle left) and EMUJ225914.55-321343.4 (middle right) fit the profile of FR I GRGs with jets on only one side. In the case of the former, there is a possibility that the radio emission on the southern side belongs to the source and there is simply a disconnect between the host and the jets. The latter however visibly displays a one-sided jet. There are two possibilities for this phenomenon: (i) the missing jet is simply too faint to be observed due to an inclined view or (ii) the source is part of a galaxy cluster. If the GRG falls into the cluster, the relativistic plasma bends and appears to be emitted on one side.

The source EMUJ230616.93-333358.8 (bottom left) can be considered unique due to the

location of bright radio emissions on its jets. Conventionally, it would be classified as an FR II GRG, however, the absence of lobes at the end of its jets may suggest otherwise.

The most unique source in this GRG sample is EMUJ225523.20-341811.4 (bottom right). From Figure 16, it is immediately noticeable that this source displays an incoherent structure. Based on the postage stamp, this source also seems to be located in a region where we see several multiple bright point-like radio sources surrounding it. EMUJ225523.20-341811.4 itself does not show a strong radio emission in its central region and its irregular radio “cloud” makes it difficult to discern its nature. Further radio observations with higher resolutions are required to reveal the complete morphology of these sources.

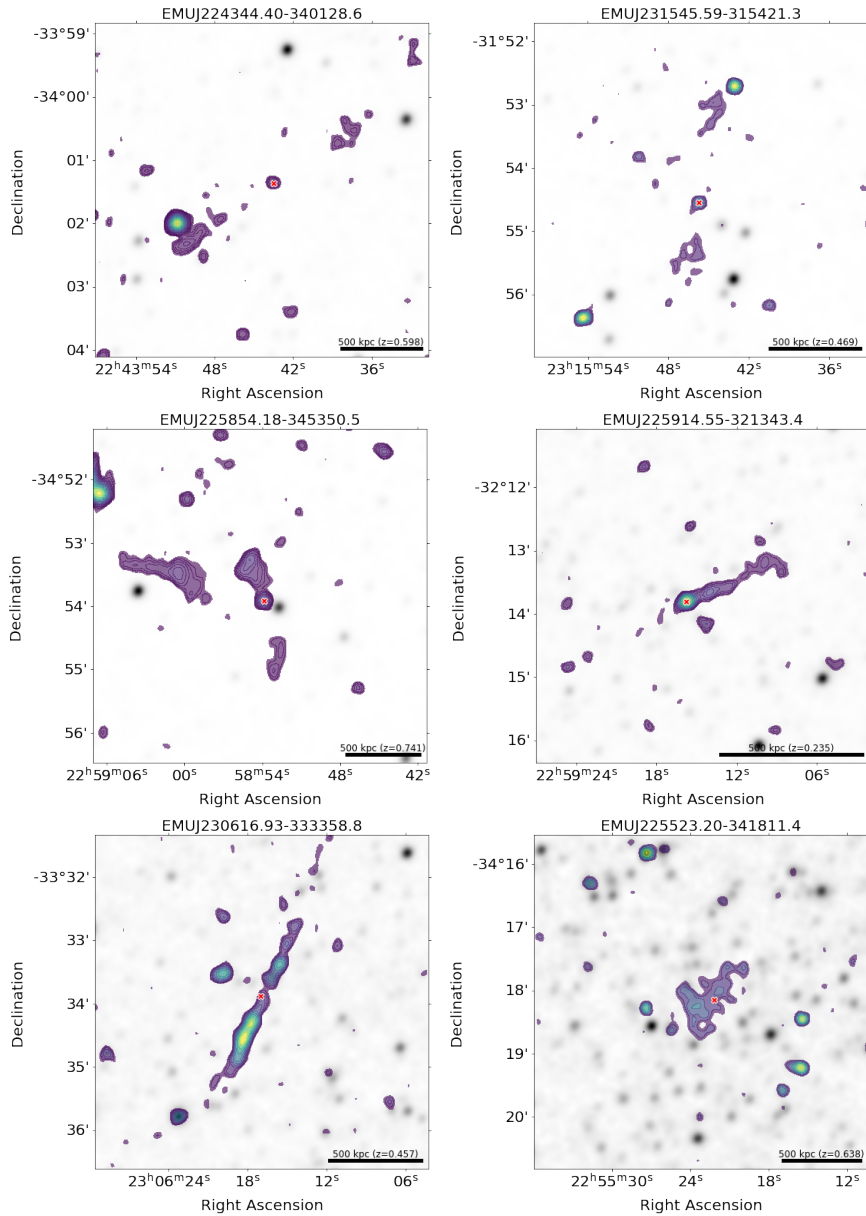


Figure 16: Postage stamps of GRGs with ambiguous morphologies.

4.3 Comparison with WISE AGN

4.3.1 Angular Size

As mentioned in Section 4.1.1, the angular sizes and redshifts of the sources were the two necessary parameters to classify them as GRGs. It is important to note that the limiting factor of this classification is the redshift, as this value is not available for all 39812 sources. In fact, taking only the angular sizes into consideration, there are a total of 473 sources that show extended jet structures (angular size > 35 arcsec, i.e. almost twice the radio beam size). Among them, all 63 GRGs and only 25 WISE AGN belong to this group. This brings up the issue of having extended AGN sources in the sample that do not possess redshifts or WISE colours in order to classify them as such, which ultimately limits our sample size. As it stands, it is very probable that there are more than 63 GRGs in the G23 field.

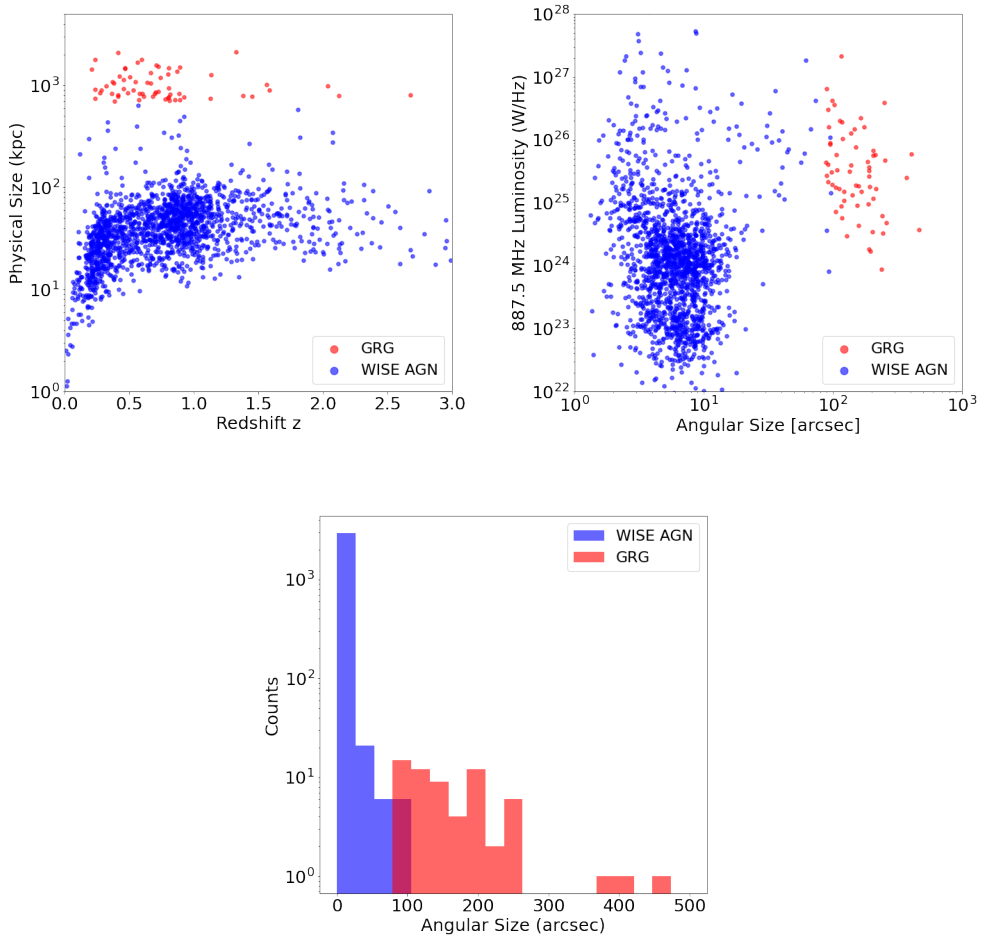


Figure 17: Top left: the physical sizes of both samples as a function of their redshifts; top right: the distribution of the 887.5 MHz radio luminosity of both samples as a function of their angular size; Bottom: the angular size distribution of both samples.

The most obvious difference between GRGs and WISE AGN is the size of their radio jets,

with a threshold of ‘physical size $> 0.7 \text{ Mpc}$ ’ used to identify GRGs. Figure 17 (top left) shows that the distribution of jet sizes for WISE AGN forms a somewhat smooth curve with increasing redshift, except for a few dozen outliers with physical sizes between 100 and 1000 kpc. GRGs are naturally located at the top of this distribution, however, the disparity between the two distributions is astounding.

Figure 17 (top right) shows us another fascinating distribution. Despite having large jet sizes, the radio luminosities of GRGs do not scale accordingly. On average, GRGs do indeed display higher radio luminosities than WISE AGN, however, the existence of brighter WISE AGN implies that the sizes of the radio jets are not solely dependent on the strength of their central engines, but also external factors as stated in Section 2.3.6.

4.3.2 Host galaxy properties

(a) WISE colours

In addition to identifying AGN, the AllWISE colours can also be used to categorize AGN according to their expected activity. The criteria used for this classification were obtained from [Gürkan et al. \(2014\)](#), who showed that AGN of different accretion modes (LERGs and HERGs) show different mid-IR colours. Moreover, [Dabhade et al. \(2020b\)](#) used the WISE colours to classify GRGs samples from the National Radio Astronomy Observatory - Very Large Array (NRAO VLA) sky surveys as part of the SAGAN project.

In our case, our entire WISE AGN sample, and 8 GRGs, lie above the $\text{W1-W2} = 0.7$ cut (see Figure 11), which makes it difficult to correctly classify them, as this area is mainly dominated by QSOs and HERGs (i.e. NLRGs and BLRGs). On the other hand, there are 39 GRGs located below this cut. The following classifications have been made according to the relevant criteria (Figure 3; [Mingo et al. 2016](#)):

- 25 GRGs are located between $1.6 < \text{W2} - \text{W3} < 3.4$. These sources are classified as star-forming galaxies and LERGs and are labelled as having spiral structures.
- 14 GRGs are at regions with $\text{W2} - \text{W3} > 3.4$. These sources are classified as starburst galaxies and ultra-luminous infrared giant radio galaxies (ULIRGs).

It is important to note that these classifications are based on different samples from [Mingo et al. \(2016\)](#), and not every aspect of it may apply to our GRG sample. This classification is also meant to serve as a rough guide because AGN, similar to normal galaxies do not fall into clear-cut categories, and not all types of AGN are successfully covered with commonly used mid-IR colour-colour diagnostics.

(b) K band magnitude

For this section, we first look at the distribution of the K-band magnitudes of both samples. The K-band has a small sensitivity towards recent star formation activity and dust extinction due to its infrared nature. This enabled [Kodama & Bower \(2003\)](#) to transform the luminosity function to a stellar mass function for two galaxy clusters 3C

336 and Q1335+28 with redshifts $z \sim 1$, which were then found to be similar to the stellar mass functions of the 2MASS/LCRS local galaxy clusters.

In our case, Figure 18 shows that the K-band magnitude of both samples show similar distributions and table 3 shows the mean K-band magnitude values of both samples with their standard error. We can see that both samples have similar K-band magnitudes, with GRGs having a lower magnitude value, indicating that they are generally brighter in the near-infrared compared to WISE AGN. This result implies that an older, redder stellar population exists in GRGs.

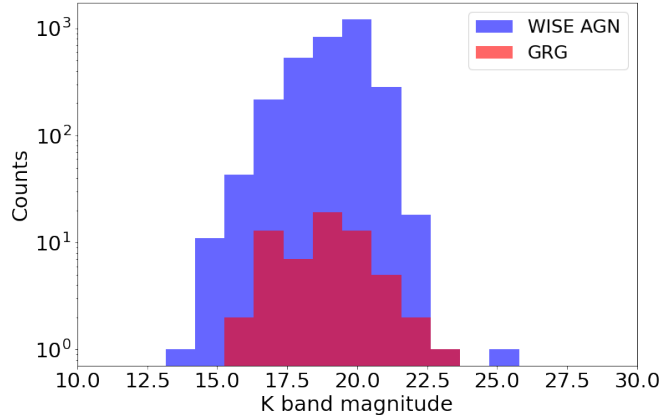


Figure 18: The K-band magnitude distribution.

Quantity	GRG	WISE AGN
Mean K-band magnitude	18.814 ± 0.205	19.180 ± 0.021

Table 3: The mean K-band magnitudes of WISE AGN and GRGs.

(c) Optical colours

Optical magnitudes and colours can also be utilized to identify the morphology of galaxies. The g-r magnitude is an optical colour band that provides information on the recent star formation rate of a galaxy based on its “redness”, where galaxies with higher g-r values are redder and have a lower star formation rate². Figure 19 (left) shows the relationship between the g-r band magnitude and the absolute r-band magnitude, with a colour cut (see Equation 3) by Sridhar (2012), and the relationship between the g-r band magnitude and the stellar mass of both samples (right):

$$(g - r)_{cut} = 0.15 - 0.03R \quad (3)$$

This colour cut establishes a threshold for the “redness” of galaxies, where sources above the line are considered “red” and sources below the line are considered “blue”. This colour distinction also enables us to sort galaxies into morphological groups (see Hubble,

²<https://skyserver.sdss.org/dr1/en/proj/advanced/color/definition.asp>

(1926), with red galaxies being elliptical galaxies (containing an older stellar population) and blue galaxies being spiral galaxies (containing a younger stellar population).

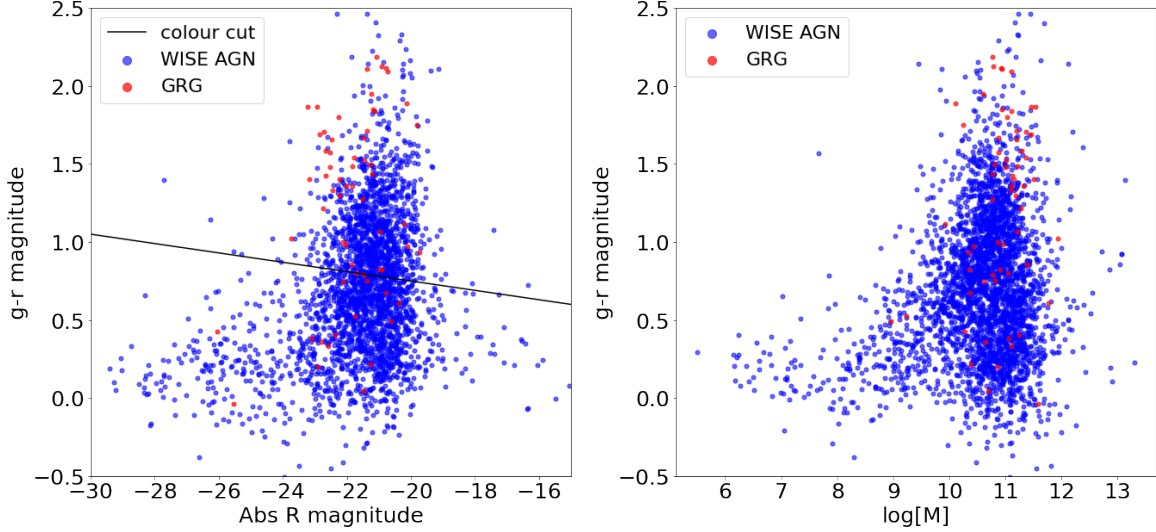


Figure 19: Left: g-r band magnitude against absolute R-band magnitude; Right: g-r band magnitude against the stellar mass (values given in terms of \log_{10}).

From Figure 19, we can immediately observe that the two distributions look very similar, which indicates that the r-band broadly traces the stellar populations of galaxies. Taylor et al. (2014) explains that the distinction between “red” and “blue” galaxies become obscured for low stellar mass values, i.e. lower than $\log[M] \sim 9.5$. Fortunately, most GRGs in our sample exceed this threshold and thus this distinction is relevant.

Based on their positions with respect to the colour cut in Figure 19 (left), the majority of our GRGs are considered “red galaxies”, which implies that they contain an older stellar population. This result is backed up by their mean K-band magnitude (see Table 3) and their stellar mass values, which are on the higher end of the distribution, as seen in Figure 19 (right). The existence of “blue” GRGs is also supported by the star-forming GRG classification obtained from the WISE colours in Section 4.3.2.

(d) Star formation rate and stellar mass

The star formation rate of a galaxy is the rate at which new stars are born each year and is measured in units of solar masses per year (M_\odot/yr), and the stellar mass of a galaxy is the sum of masses of star populations in a galaxy which traces the galaxy formation process. These two parameters aid in studying the evolution of galaxies, and comparing them for our two galaxy populations will give us some useful insight into their natures. Obtaining these parameters is no easy feat, therefore we only have a handful of sources for which these values have been estimated according to the methods described in Section 3.2. Table 4 shows the number of sources for which these values exist.

Quantity	GRG	WISE AGN
Counts (star formation rate)	32 (50%)	844 (16%)
Counts (stellar mass)	62 (98%)	3165 (61%)

Table 4: Number of GRGs and WISE AGN with star formation rates and stellar masses.

Figure 20 shows the relationship between the star formation rate and the stellar mass of both samples. In the left diagram, a familiar trend can be seen: the mean stellar mass values of GRGs are on the higher end compared to WISE AGN, albeit not by a large amount (see Table 5). One possibility is that some of these GRGs are located within galaxy clusters, therefore the estimation of their stellar mass was influenced by additional mass from these clusters. The star formation rates on the other hand show a more interesting result: GRGs show much lower star formation rates than WISE AGN (for a given similar stellar mass), by a large margin. This general trend implies that the AGN activity that produces these large jets reduces the overall star formation rate of the galaxy.

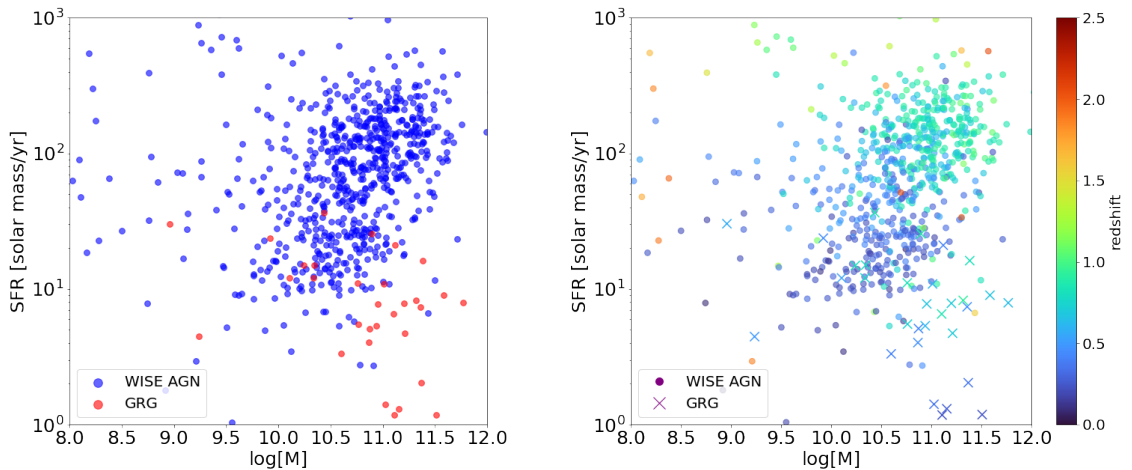


Figure 20: Left: The distribution of star formation rates as a function of their stellar mass for WISE AGN and GRGs; Right: The same distribution as the left, colour-coded by the redshifts of the sources.

A surprising observation is that most WISE AGN, and almost half of all GRGs show starburst-like star formation rates (i.e. $SFR > 10 M_{\odot}/\text{yr}$; [Muxlow et al. 2006](#)). This could potentially be attributed to the high uncertainty when estimating these star formation rate values, however optical colours seen in Section 4.3.2 show that “blue” GRGs do indeed exist in our sample, which could be an indicator for these high star formation rates. The mean star formation rates in Table 5 and the WISE colour classifications in Section 4.3.2 further support this result. A large uncertainty still exists, but even at the lowest end, the mean star formation rate of GRGs exceeds the threshold for a starburst-like classification. It is possible that recent star formation was triggered by past merger activities ([Ku  micz et al., 2019](#)), which is further evidence that GRGs exist within galaxy clusters.

Figure 20 (right) shows the same distribution as the left diagram, colour-coded by the redshift values. The colour distribution shows the same trend for both samples, where the star formation rates increases with increasing redshifts (blue to green). This result matches our current understanding of the relationship between these two parameters, i.e. the star formation rates of galaxies increase with redshift up to $z \sim 2$, where the highest star formation rates are observed (see [Lehnert et al., 2015](#)).

Quantity	GRG	WISE AGN
Mean star formation rate (M_{\odot}/yr)	19.212 ± 8.912	135.994 ± 6.868
Mean stellar mass [$\log(M_{\odot})$]	10.906 ± 0.066	10.573 ± 0.015

Table 5: The mean star formation rate and stellar mass values.

Additionally, a Kolmogorov–Smirnov test (K-S test; see [Massey 1951](#)) was conducted as a goodness-of-fit test to compare these parameters for GRGs and WISE AGN. The purpose of this test is to check if the underlying probability distributions of star formation rates and stellar masses of the two samples differ from each other. The interpretation of this test is as follows: (i) the closer the statistic value is to 0, the higher the probability of both samples being drawn from the same distribution; (ii) if the p-value is less than the chosen significance level, then the null hypothesis that the two samples were drawn from the same distribution is rejected.

K-S Test	Statistic	p-value
Star formation rate	0.715	6.661×10^{-16}
Stellar mass	0.284	7.747×10^{-5}

Table 6: The K-S Test results for star formation rate and stellar mass.

From the test results in Table 6, we can see that based on a chosen confidence level of 95%, the p-values are much less than 0.05 for both cases. Therefore, we can reject the null hypothesis that the two samples are drawn from the same distribution.

4.4 Comparison to the literature

In this section, I evaluate and discuss our results with regard to the findings in the literature to look for commonalities and differences.

Our GRG sample primarily shows FRII morphologies, with a few showing FRI morphologies, and some showing ambiguous structures (see Section 4.2.1). This result is verified by multiple studies (e.g. [Ishwara-Chandra & Saikia 1999](#), [Kuźmicz et al. 2018](#), [Dabhade et al. 2020a](#), and [Dabhade et al. 2020b](#)), where at least 90% of the GRGs in the respective studies showed FRII morphologies.

Our optical colour analysis in Figure 19 shows that almost all GRGs and a high concentration of typical-size AGN lie in a similar r-band colour magnitude range. [Dabhade et al. \(2020b\)](#) showed that this ranges from ~ -19 to -25 , which fits the range of our results. However, this indicates that optically, GRGs and typical-sized AGN are not very different.

In Section 4.3.2, we also established that more than half of all GRGs are “red”, which suggests that they are hosted by elliptical galaxies. This result is further supported by Dabhade et al. (2020a), who found that most of the GRGs in their sample had elliptical host galaxies, with some having quasar hosts and none having spiral hosts.

We used mid-IR classification criteria presented by Gürkan et al. (2014) to identify the excitation mode of our GRG sample. This classification was further verified by Mingo et al. (2016), O’Sullivan et al. (2015) and Whittam et al. (2018), and was later used by Dabhade et al. (2017) as well as Simonte et al. (2022) for the same purpose. To that end, our classifications match exactly. GRGs located between $1.6 < W2 - W3 < 3.4$ are classified as star-forming galaxies and LERGs with spiral structures, and GRGs are at regions with $W2 - W3 > 3.4$ are classified as starburst galaxies and ultra-luminous infrared giant radio galaxies (ULIRGs). However, these findings somewhat contradict our optical results, which indicate that the majority of our GRGs have elliptical hosts. The reason for this contradiction is simply the different samples used by Mingo et al. (2016) for their classifications, which involve different methods of sample selection.

Simonte et al. (2022) also studied the star formation rate and stellar mass distributions of GRGs and typical-size AGN. Comparing their results to ours, we can see that our sources show a similar distribution, where almost all of our GRGs display large stellar masses ($> 10^{10.5} M_{\odot}$). This result indicates that GRGs are essentially dead systems hosted by luminous elliptical galaxies populated by giant stars (Dabhade et al. 2017, Machalski et al. 2001, Clarke et al. 2017, Seymour et al. 2020). These GRGs should theoretically be devoid of star formation, there are rare cases where GRGs with spiral host galaxies have been found (Mao et al., 2014). Kuźmicz et al. (2019) and Zovaro et al. (2021) have also shown that GRGs can also contain ‘intermediate’ stellar populations, and that star formation in GRGs is not impossible. In fact, this finding supports our results in Section 4.3.2, where we have shown that our GRGs have star formation rates larger than $10 M_{\odot}/\text{yr}$.

5 Summary and conclusion

This thesis aims to understand the nature of giant radio galaxies (GRGs) and how they compare to typical-size AGN. To this end, I used the radio data and the value-added radio catalogue from the ASKAP survey of the G23 field ([Gürkan et al., 2022](#)), which is a $\sim 50 \text{ deg}^2$ region in the southern hemisphere. The radio observations were conducted at 887.5 MHz, covering a wide 82.7 deg^2 field. Alongside the radio data, a multi-wavelength catalogue containing data sets from the GAMA collaboration was used. These data sets cover a wide range of the electromagnetic spectrum, from ultraviolet to far-infrared.

The GRGs were selected based on the physical size of their radio jets ($>0.7 \text{ Mpc}$), which I calculated using their angular sizes and redshifts and the typical-sized AGN were selected using AllWISE colours ($W1-W2 \geq 0.7$). A total of **63** GRGs and **5217** WISE AGN were identified using these methods. By comparing the properties of the two samples, we can gain insight into the nature of GRGs and their host galaxies. The comparison yielded the following results:

- WISE colours indicate that our GRG sample consists of mostly LERGs and star-forming galaxies, while the typical-sized AGN sample consists of mostly HERGs.
- The radio luminosities of GRGs do not scale with their jet sizes. Despite having jets that span up to Mpc scales, their radio luminosities are only slightly higher than that of typical-sized AGN.
- The mean K-band magnitude of GRGs is lower than WISE AGN, indicating that GRGs contain a redder, older stellar population.
- The g-r band magnitude shows that most GRGs are considered “red”, which put them into the elliptical morphology group. There also exist “blue” GRGs, which classify them as spiral galaxies.
- The stellar masses of GRGs are on the higher end of the distribution, indicating that their host galaxies are more massive than typical-sized AGN.
- The star formation rates of GRGs are significantly lower than typical-sized AGN. This suggests that the powerful jets seen in GRGs impact their host galaxies a lot more than the jets seen in typical-size AGN. Another reason for this difference may be due to the difference between the morphology of galaxies in both samples, where GRGs have a higher tendency to have elliptical hosts, and typical-size AGN have a higher tendency to have spiral hosts.
- The results of the two sample K-S test for the stellar masses and star formation rates of the samples indicate that GRGs and typical-size AGN are not drawn from the same distribution. The accuracy of this result could be improved with a larger GRG sample size, however, as it stands, this result suggests that GRGs are intrinsically different objects than typical-size AGN.

Each analysis utilises different data sets to study different properties of AGN, and yet, many of the results obtained from our analysis support each other. For example, the K-band and g-r band luminosities both show that GRGs are situated at the tail end of galaxy evolution as they consist of mostly old, red stars. The WISE colours suggest that most GRGs are LERGs, which support the existence of large extended jets caused by their jet-mode accretion. Furthermore, the surprisingly high star formation rates seen in some GRGs are also backed up by the existence of “blue” GRGs from optical colours. Comparing the results of our analysis with other studies also provided us with some insight into the complexity of AGN, as there are multiple instances where some of our results are contradictory to other results, and uncovering the nature of GRGs and AGN, in general, is no easy feat.

Therefore, the results obtained in this thesis show that there is still much to be desired. With the help of next-generation radio surveys with higher resolutions, we will be able to obtain much deeper data that could allow us to compile larger samples of GRGs. Better multi-wavelength data and optical spectroscopy will also provide us with more accurate data to gain deeper insights into the nature of GRGs and galaxy evolution as a whole.

6 References

- Aceituno J., et al., 2013, [A&A](#), 552, A31
- Aird J., et al., 2010, [MNRAS](#), 401, 2531
- Baldry I. K., et al., 2012, [MNRAS](#), 421, 621
- Baldwin J. A., Phillips M. M., Terlevich R., 1981, [PASP](#), 93, 5
- Bellstedt S., et al., 2020, [MNRAS](#), 496, 3235
- Bianchi S., Maiolino R., Risaliti G., 2012, [Advances in Astronomy](#), 2012, 1
- Boquien Burgarella, D. Roehlly, Y. Buat, V. Ciesla, L. Corre, D. Inoue, A. K. Salas, H. 2019, [A&A](#), 622, A103
- Bourne N., et al., 2016, [MNRAS](#), 462, 1714
- Clarke et al., 2017, [A&A](#), 601, A25
- Condon J. J., 1992, [ARA&A](#), 30, 575
- Condon J. J., Cotton W. D., Greisen E. W., Yin Q. F., Perley R. A., Taylor G. B., Broderick J. J., 1998, [AJ](#), 115, 1693
- Dabhade P., Gaikwad M., Bagchi J., Pandey-Pommier M., Sankhyayan S., Raychaudhury S., 2017, [MNRAS](#), 469, 2886
- Dabhade et al., 2020a, [A&A](#), 635, A5
- Dabhade et al., 2020b, [A&A](#), 642, A153
- Dabhade P., Saikia D. J., Mahato M., 2022, arXiv e-prints, p. [arXiv:2208.02130](#)
- Dermer C. D., Giebels B., 2016, [Comptes Rendus Physique](#), 17, 594
- Doré O., et al., 2016, Science Impacts of the SPHEREx All-Sky Optical to Near-Infrared Spectral Survey: Report of a Community Workshop Examining Extragalactic, Galactic, Stellar and Planetary Science, <https://arxiv.org/abs/1606.07039>
- Driver S. P., et al., 2011, [MNRAS](#), 413, 971
- Falomo R., Pian E., Treves A., 2014, [A&A Rev.](#), 22
- Fanaroff B. L., Riley J. M., 1974, [MNRAS](#), 167, 31P
- Ferreira L., et al., 2022, Panic! At the Disks: First Rest-frame Optical Observations of Galaxy Structure at $z > 3$ with JWST in the SMACS 0723 Field, <https://arxiv.org/abs/2207.09428>
- Gardner J. P., et al., 2006, [Space Science Reviews](#), 123, 485

- Gopal-Krishna Wiita P. J., Saripalli L., 1989, [MNRAS](#), **239**, 173
- Gordon Y. A., et al., 2016, [MNRAS](#), **465**, 2671
- Gürkan G., Hardcastle M. J., Jarvis M. J., 2014, [MNRAS](#), **438**, 1149
- Gürkan G., et al., 2015, [MNRAS](#), **452**, 3776
- Gürkan G., et al., 2019, [A&A](#), **622**, A11
- Gürkan G., et al., 2022, [MNRAS](#), **512**, 6104
- Gürkan G., Croston J., Hardcastle M. J., Mahatma V., Mingo B., Williams W. L., 2021, [Galaxies](#), **10**, 2
- Hale C. L., et al., 2021, [Publications of the Astronomical Society of Australia](#), **38**
- Hardcastle et al., 2019, [A&A](#), **622**, A12
- Harrison C., 2014, PhD thesis, Durham University, UK, <https://ui.adsabs.harvard.edu/abs/2014PhDT.....357H>
- Heckman T. M., Best P. N., 2014, [ARA&A](#), **52**, 589
- Hine R. G., Longair M. S., 1979, [MNRAS](#), **188**, 111
- Ho L. C., Filippenko A. V., Sargent W. L. W., 1997, [ApJ](#), **487**, 568
- Hubble E. P., 1926, [ApJ](#), **64**, 321
- Hurley-Walker N., et al., 2016, [MNRAS](#), **464**, 1146
- Intema H. T., Jagannathan P., Mooley K. P., Frail D. A., 2017, [A&A](#), **598**, A78
- Ishwara-Chandra C. H., Saikia D. J., 1999, [Monthly Notices of the Royal Astronomical Society](#), **309**, 100
- Jones M., Adams D., Lambourne R., Adams D., 2004, An Introduction to Galaxies and Cosmology. S 282, Open University, <https://books.google.de/books?id=36K1PfetZegC>
- Kalfountzou E., et al., 2014, [MNRAS](#), **442**, 1181
- Kerr R. P., 1963, [Phys. Rev. Lett.](#), **11**, 237
- Khachikian E. Y., Weedman D. W., 1974, [ApJ](#), **192**, 581
- Kodama T., Bower R., 2003, [MNRAS](#), **346**, 1
- Kuźmicz A., Czerny B., Wildy C., 2019, [A&A](#), **624**, A91
- Kuźmicz A., Jamrozy M., Bronarska K., Janda-Boczar K., Saikia D. J., 2018, [The Astrophysical Journal Supplement Series](#), **238**, 9

- Laing R. A., Jenkins C. R., Wall J. V., Unger S. W., 1994, in Bicknell G. V., Dopita M. A., Quinn P. J., eds, Astronomical Society of the Pacific Conference Series Vol. 54, The Physics of Active Galaxies. p. 201
- Lauer T. R., et al., 2021, [ApJ](#), 906, 77
- Lehnert M., Nesvadba N., van Driel W., Le Tiran L., Matteo P., 2015, [A&A](#), 577
- Liske J., et al., 2015, [MNRAS](#), 452, 2087
- Machalski Jamrozy, M. Zola, S. 2001, [A&A](#), 371, 445
- Mack K. H., Klein U., O'Dea C. P., Willis A. G., Saripalli L., 1998, [A&A](#), 329, 431
- Malarecki J. M., Jones D. H., Saripalli L., Staveley-Smith L., Subrahmanyan R., 2015, [MNRAS](#), 449, 955
- Mao M. Y., et al., 2014, [MNRAS](#), 446, 4176
- Massey F. J., 1951, Journal of the American Statistical Association, 46, 68
- Matteo T. D., Springel V., Hernquist L., 2005, [Nature](#), 433, 604
- Mauch T., Murphy T., Buttery H. J., Curran J., Hunstead R. W., Piestrzynski B., Robertson J. G., Sadler E. M., 2003, [MNRAS](#), 342, 1117
- Messier C., Niles P., 1981, The Messier catalogue of Charles Messier, <https://www.nasa.gov/content/goddard/hubble-s-messier-catalog>
- Mingo B., et al., 2016, [MNRAS](#), 462, 2631
- Mingo B., et al., 2019, [MNRAS](#), 488, 2701
- Mohan N., Rafferty D., 2015, PyBDSF: Python Blob Detection and Source Finder, Astrophysics Source Code Library, record ascl:1502.007 (ascl:1502.007)
- Muxlow T. W. B., Beswick R. J., Richards A. M. S., Thrall H., 2006, Starburst Galaxies, <https://arxiv.org/abs/astro-ph/0611951>
- Norris R. P., et al., 2011, [Publications of the Astronomical Society of Australia](#), 28, 215
- Oei M. S. S. L., et al., 2022, [A&A](#), 660, A2
- O'Sullivan S. P., Gaensler B. M., Lara-López M. A., van Velzen S., Banfield J. K., Farnes J. S., 2015, [ApJ](#), 806, 83
- Peterson B. M., 1997, An Introduction to Active Galactic Nuclei. Cambridge University Press, [doi:10.1017/CBO9781139170901](https://doi.org/10.1017/CBO9781139170901)
- Proust D., Yegorova I., Saviane I., Ivanov V., Bresolin F., Salzer J., Capelato H., 2015, [MNRAS](#), 452

- Schmidt M., Green R. F., 1983, [ApJ](#), **269**, 352
- Seyfert C. K., 1943, [ApJ](#), **97**, 28
- Seymour N., et al., 2020, [Publications of the Astronomical Society of Australia](#), **37**, e013
- Shang Z., et al., 2005, [ApJ](#), **619**, 41
- Shapiro S. L., Teukolsky S. A., 1983, Black holes, white dwarfs, and neutron stars : the physics of compact objects
- Shimwell T. W., et al., 2022, [A&A](#), **659**, A1
- Shirley R., et al., 2021, [MNRAS](#), **507**, 129
- Simonte M., Andernach H., Brüggen M., Schwarz D. J., Prandoni I., Willis A. G., 2022, [MNRAS](#), **515**, 2032
- Sridhar S., 2012, PhD thesis, [doi:10.13140/2.1.3286.6084](#)
- Stern D., et al., 2012, [ApJ](#), **753**, 30
- Subrahmanyam R., Saripalli L., Hunstead R. W., 1996, [MNRAS](#), **279**, 257
- Tadhunter C., 2016, [A&A Rev.](#), **24**
- Taylor M. B., 2005, in Shopbell P., Britton M., Ebert R., eds, Astronomical Society of the Pacific Conference Series Vol. 347, Astronomical Data Analysis Software and Systems XIV. p. 29
- Taylor E. N., et al., 2014, [MNRAS](#), **446**, 2144
- Whittam I. H., Prescott M., McAlpine K., Jarvis M. J., Heywood I., 2018, [MNRAS](#), **480**, 358
- Wiita P. J., Rosen A., Gopal-Krishna Saripalli L., 1989, in Meisenheimer K., Röser H.-J., eds, Hot Spots in Extragalactic Radio Sources. Springer Berlin Heidelberg, Berlin, Heidelberg, pp 173–178
- Woltjer L., 1959, [ApJ](#), **130**, 38
- Zovaro H. R. M., Riseley C. J., Taylor P., Nesvadba N. P. H., Galvin T. J., Malik U., Kewley L. J., 2021, [MNRAS](#), **509**, 4997

A Appendix

A.1 Postage Stamps

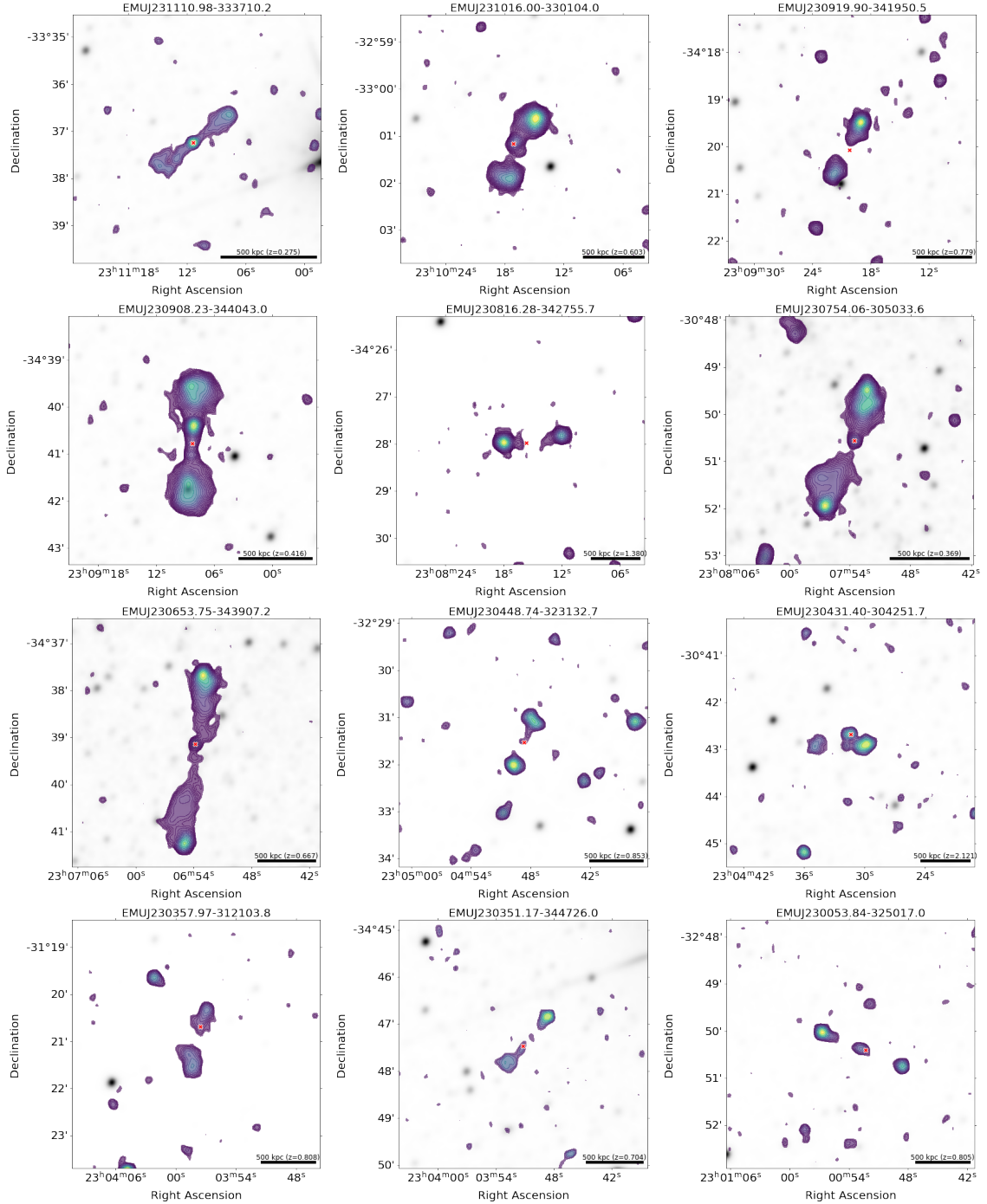


Figure 21: Postage Stamps of GRGs (1-12)

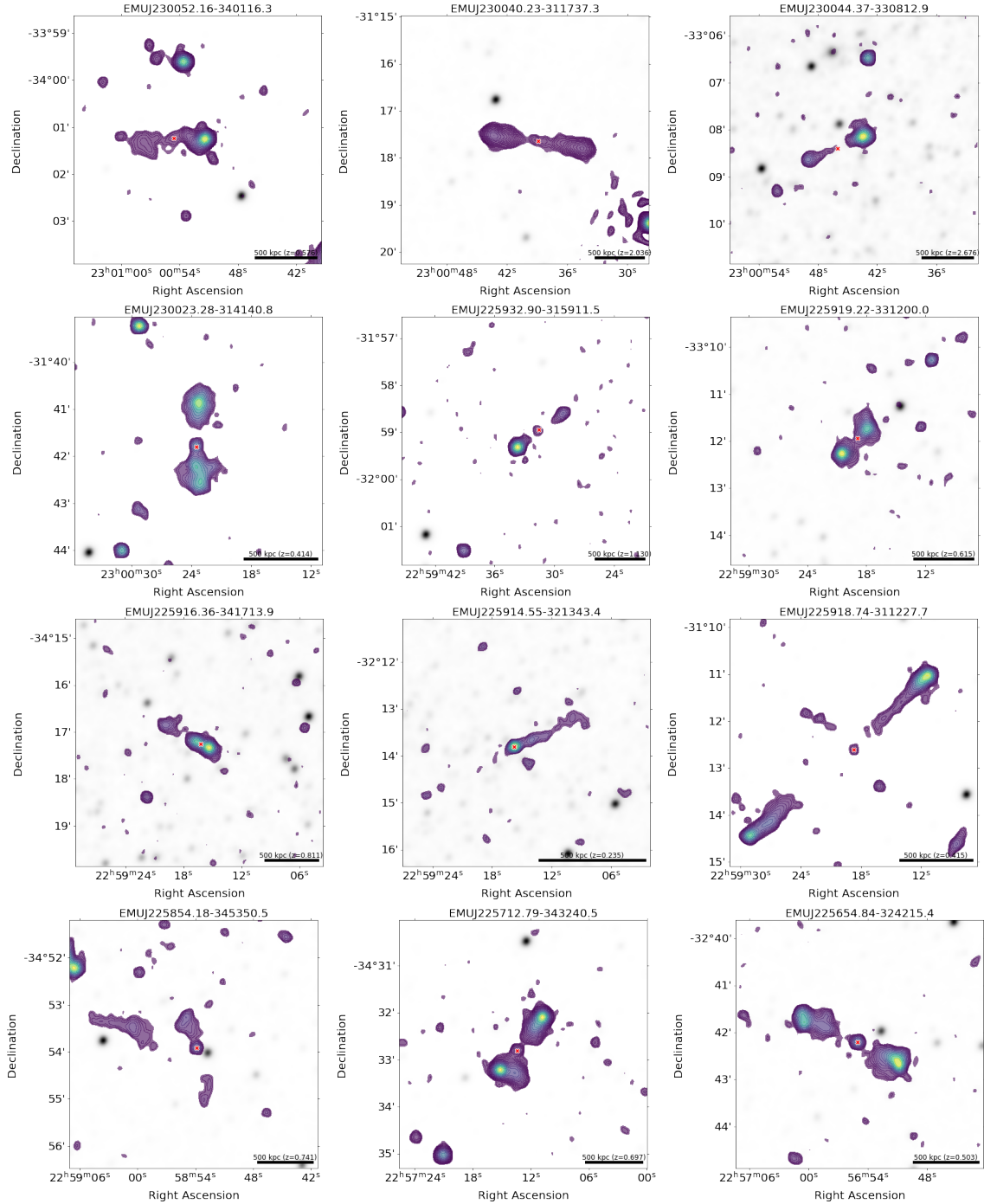


Figure 22: Postage Stamps of GRGs (13-24)

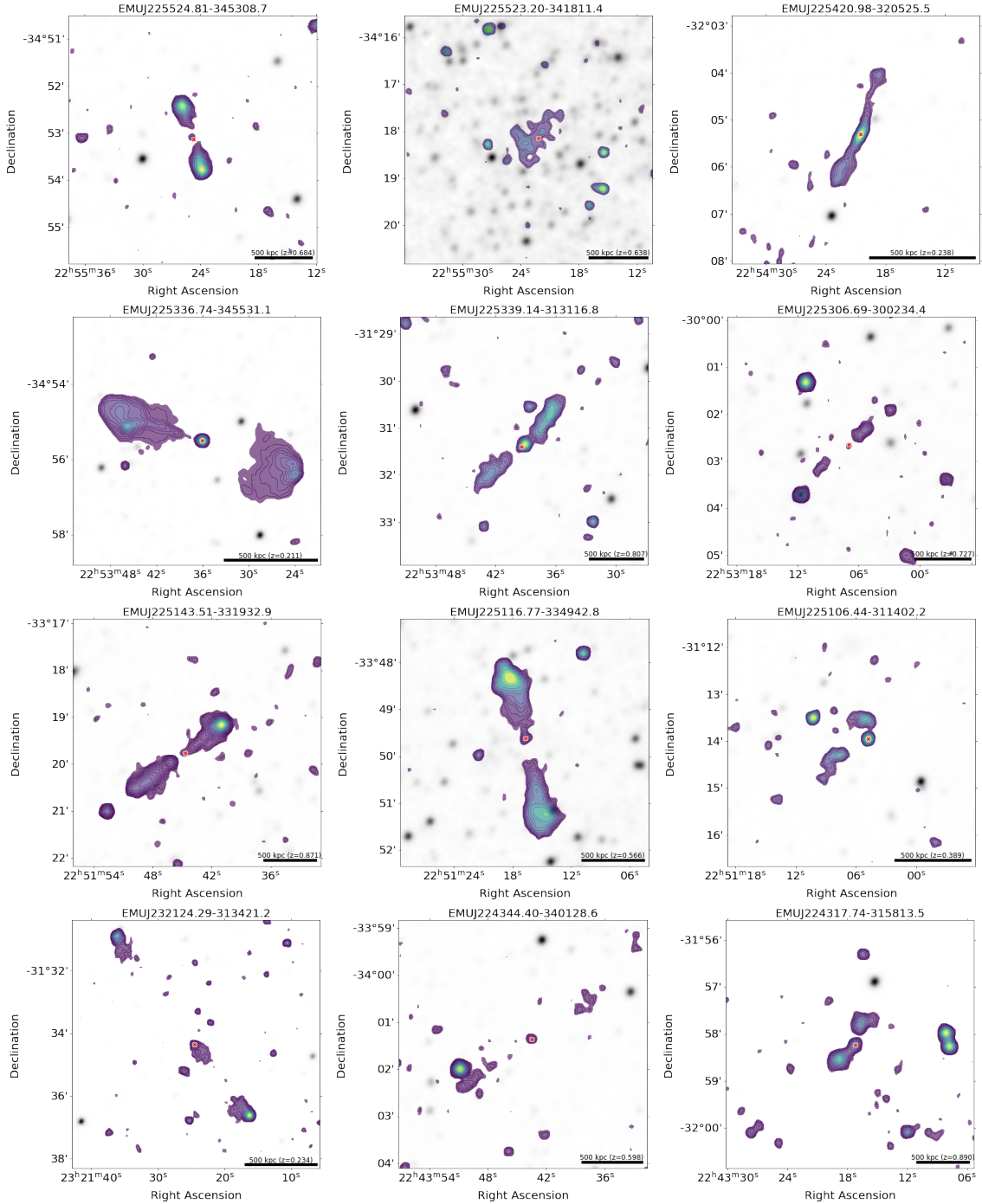


Figure 23: Postage Stamps of GRGs (25-36)

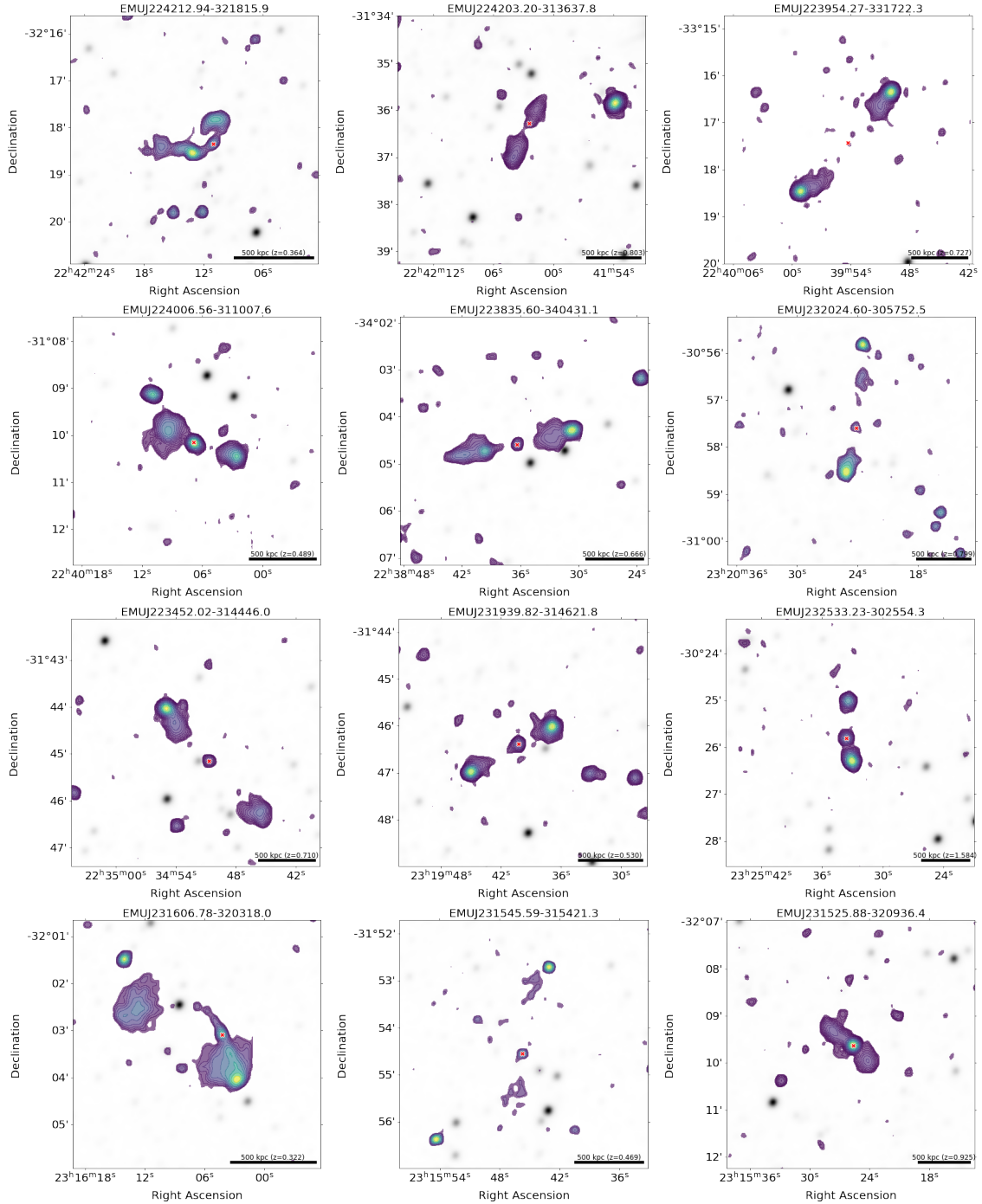


Figure 24: Postage Stamps of GRGs (37-48)

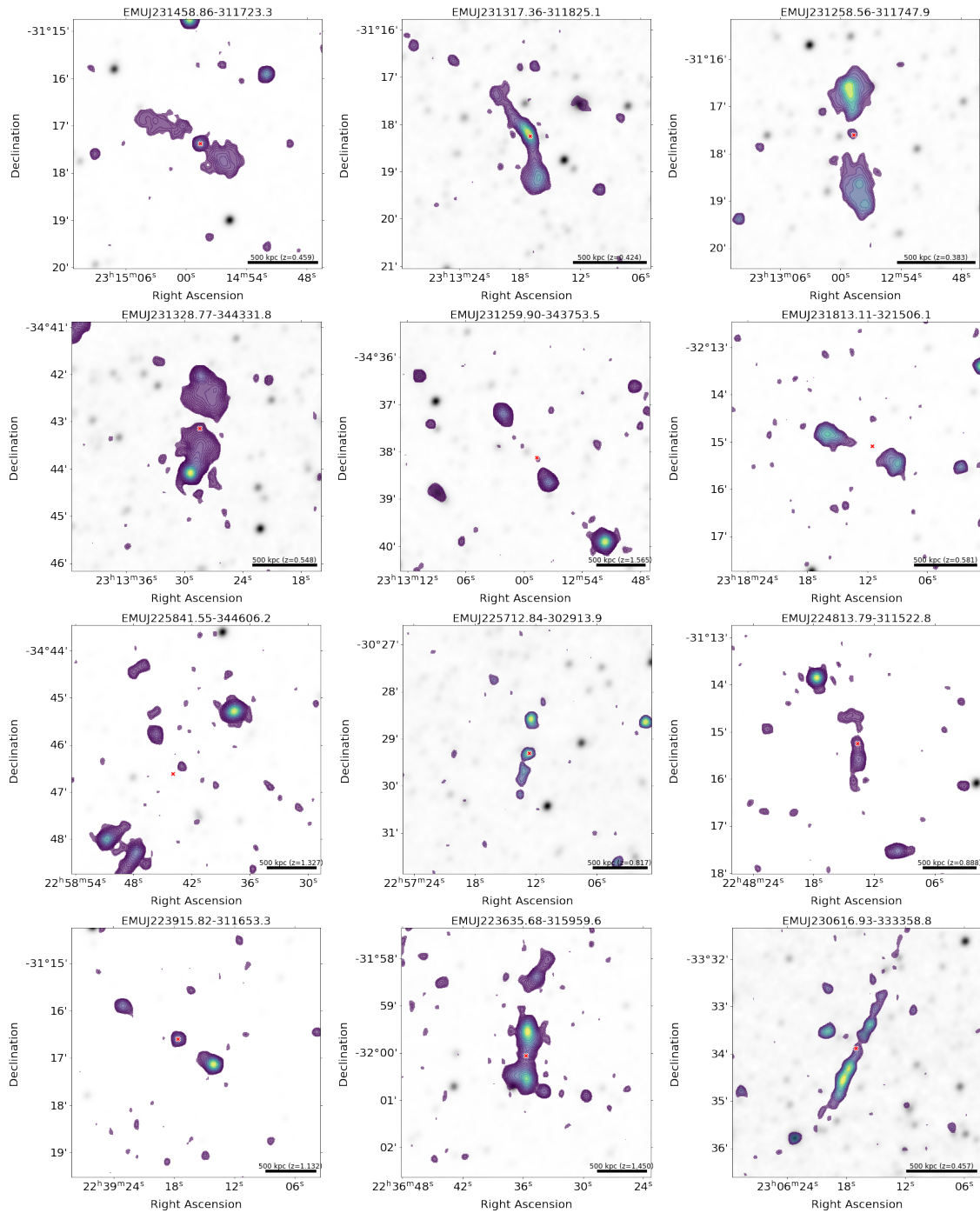


Figure 25: Postage Stamps of GRGs (49-60)

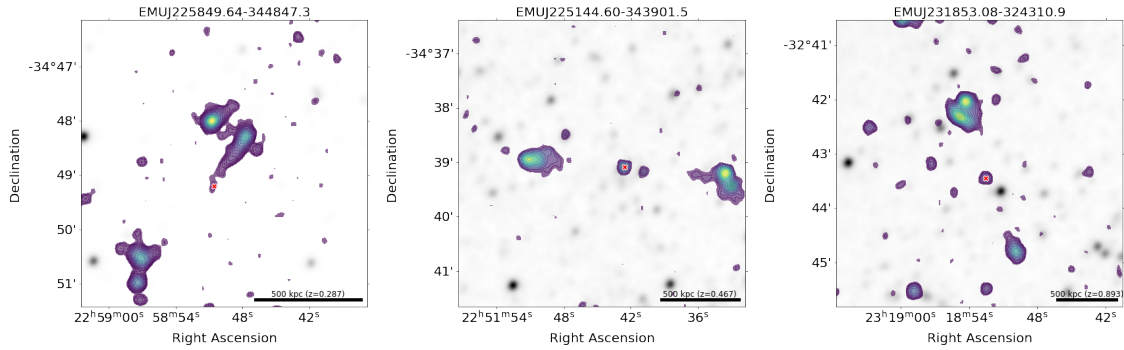


Figure 26: Postage Stamps of GRGs (61-63)

A.2 List of GRG

Source name [1]	z [2]	Flux density [3]	r mag [4]	SFR [5]	Stellar mass [6]	Morphology [7]
EMUJ231110.98-333710.2	0.275	0.0072	18.578	1.309	11.156	FR II
EMUJ231016.00-330104.0	0.603	0.0753	22.049		10.364	FR II
EMUJ230919.90-341950.5	0.779	0.0335	23.771	12.066	10.339	FR II
EMUJ230908.23-344043.0	0.416	0.2168	20.618	3.324	10.601	FR II
EMUJ230816.28-342755.7	1.38	0.0322	23.766		10.383	FR II
EMUJ230754.06-305033.6	0.369	0.124	18.832	2.037	11.371	FR II
EMUJ230653.75-343907.2	0.668	0.0841	17.55	9.0	11.588	FR II
EMUJ230448.74-323132.7	0.853	0.0069	23.001	6.542	11.105	FR II
EMUJ230431.40-304251.7	2.121	0.0065	23.264		10.852	?
EMUJ230357.97-312103.8	0.808	0.0072	23.786	14.891	10.243	FR II
EMUJ230351.17-344726.0	0.704	0.0045	21.008		11.188	FR II
EMUJ230053.84-325017.0	0.805	0.0056	21.469		10.619	FR II
EMUJ230052.16-340116.3	0.576	0.0464	22.076	30.285	8.96	FR II
EMUJ230040.23-311737.3	2.036	0.0947	23.257		10.64	FR II
EMUJ230044.37-330812.9	2.676	0.0102	23.035		11.933	FR II
EMUJ230023.28-314140.8	0.414	0.0228	19.3	5.107	10.874	FR II
EMUJ225932.90-315911.5	1.13	0.0075	22.803		11.043	FR II
EMUJ225919.22-331200.0	0.615	0.0115	21.695	5.354	10.941	FR II
EMUJ225916.36-341713.9	0.811	0.0145	22.137	11.086	10.761	?
EMUJ225914.55-321343.4	0.235	0.0054	17.977	1.177	11.11	FR I
EMUJ225918.74-311227.7	0.415	0.043	19.189	21.01	11.121	FR II
EMUJ225854.18-345350.5	0.741	0.0083	22.235		11.108	FR II
EMUJ225712.79-343240.5	0.697	0.1035	22.241	4.718	11.214	FR II
EMUJ225654.84-324215.4	0.504	0.0399	20.608	4.455	9.237	FR II
EMUJ225524.81-345308.7	0.684	0.0177	21.783		10.939	FR II
EMUJ225523.20-341811.4	0.639	0.012	22.583	7.907	11.77	?
EMUJ225420.98-320525.5	0.238	0.0108	17.273	1.185	11.509	FR I
EMUJ225336.74-345531.1	0.211	0.4538	17.427		11.273	FR II
EMUJ225339.14-313116.8	0.807	0.0118	22.384		10.764	FR I
EMUJ225306.69-300234.4	0.727	0.0027	22.541		10.913	?
EMUJ225143.51-331932.9	0.871	0.0494	23.691	36.53	10.437	FR II
EMUJ225116.77-334942.8	0.566	0.039	20.626		11.107	FR II
EMUJ225106.44-311402.2	0.389	0.0059	18.833		11.464	?
EMUJ232124.29-313421.2	0.234	0.0229	18.291		10.859	FR II
EMUJ224344.40-340128.6	0.598	0.0035	21.338	10.893	11.014	?
EMUJ224317.74-315813.5	0.89	0.0079	21.477		11.251	FR II
EMUJ224212.94-321815.9	0.364	0.01	19.267	1.413	11.028	FR II
EMUJ224203.20-313637.8	0.803	0.0113	22.651	14.989	10.346	FR II
EMUJ223954.27-331722.3	0.727	0.0312	22.245	5.509	10.764	FR II
EMUJ224006.56-311007.6	0.489	0.037	19.328		11.456	FR II
EMUJ223835.60-340431.1	0.666	0.0256	21.022	7.767	10.956	FR II
EMUJ232024.60-305752.5	0.799	0.0057	22.065		10.767	FR II
EMUJ223452.02-314446.0	0.71	0.0285	21.867	7.843	11.202	FR II
EMUJ231939.82-314621.8	0.53	0.0387	22.34	12.05	10.106	FR II
EMUJ232533.23-302554.3	1.584	0.028	19.355		10.271	FR II
EMUJ231606.78-320318.0	0.322	0.0357	18.543		11.286	FR II
EMUJ231545.59-315421.3	0.469	0.0043	19.641		10.992	?
EMUJ231525.88-320936.4	0.925	0.0238	22.112	8.242	11.32	FR I
EMUJ231458.86-311723.3	0.459	0.0127	20.348	7.392	11.36	FR II
EMUJ231317.36-311825.1	0.424	0.027	18.67		11.538	FR I
EMUJ231258.56-311747.9	0.383	0.0368	19.162		11.194	FR II
EMUJ231328.77-344331.8	0.548	0.1992	20.727		11.211	FR II
EMUJ231259.90-343753.5	1.565	0.0154	22.276		11.058	FR II
EMUJ231813.11-321506.1	0.581	0.0085	21.816		10.789	FR II
EMUJ225841.55-344606.2	1.327	0.0449	23.449		10.688	?
EMUJ225712.84-302913.9	0.817	0.0026	21.777	16.174	11.386	?
EMUJ224813.79-311522.8	0.888	0.0051	22.476		10.813	?

Source name [1]	z [2]	Flux density [3]	r mag [4]	SFR [5]	Stellar Mass[6]	Morphology [7]
EMUJ223915.82-311653.3	1.132	0.0128		291.304		FR II
EMUJ223635.68-315959.6	1.45	0.0609	22.568		11.109	FR II
EMUJ230616.93-333358.8	0.457	0.0124	21.888	23.705	9.924	FR I
EMUJ225849.64-344847.3	0.287	0.0136	19.634		10.803	FR II
EMUJ225144.60-343901.5	0.467	0.0081	20.66	4.025	10.868	FR II
EMUJ231853.08-324310.9	0.893	0.0076	22.876	25.496	10.899	FR II

Table 7: List of all GRGs with important parameters. Columns: [1] Source name. [2] Reliable spectroscopic and photometric redshifts. [3] Total radio flux density (mJy). [4] Optical r-band magnitude. [5] Star formation rate of galaxies, in units of (M_{\odot}/yr) [6] Base 10 logarithmic values of the stellar mass of galaxies ($\log[M_{\star}]$), [7] Morphology of galaxies. Most sources show FR II morphology, however, there are sources that show FR I morphology and in some cases, the morphology is unclear (denoted by "?").

A.3 Python Code

A.3.1 Identifying GRGs

```

import numpy as np
import matplotlib.pyplot as plt
import astropy.units as u
from astropy.table import Table
from astropy.table import Column
from astropy.table import MaskedColumn
from astropy.cosmology import FlatLambdaCDM

cosmo = FlatLambdaCDM(H0=67.7*u.km/u.s/u.Mpc,Tcmb0=2.725*u.K,Om0=0.310)

#reading the fits table containing all data
t = Table.read('table_initial.fits')

#creating an array containing only reliable redshift values and adding them
#to the table
z = []
for i, it in enumerate(t):
    if t['Z_tilv11'][i] >= 0.002 and t['NQ_tilv11'][i] >2:
        z.append(t['Z_tilv11'][i])
    elif t['redshift_h'][i] > 0:
        z.append(t['redshift_h'][i])
    elif t['z_peak'][i] > 0 and t['science_primary'][i] == True:
        z.append(t['z_peak'][i])
    else:
        z.append(np.nan)

redshift = Column(z, name = 'z_final')
t['z_final'] = redshift

t.write('table_final.fits',overwrite=True)

#obtaining the physical sizes of the sources and adding them to the table
ADD = cosmo.angular_diameter_distance(t['z_final'])
ang_size = t['Size'] * u.arcsec
phy_size = (ADD*NS).to(u.kpc, u.dimensionless_angles())
Physical_size = Column(phy_size, name = 'Physical_Size')
t['Physical_Size'] = Physical_size

t.write('table_final.fits',overwrite=True)

```

A.3.2 Plotting the postage stamps

```

from astropy.io import fits
from astropy.wcs import WCS
from astropy.coordinates import SkyCoord
from astropy.nddata import Cutout2D
from astropy.table import Table
import numpy as np
import astropy.units as u
import matplotlib.pyplot as plt
from reproject import reproject_interp
import matplotlib.cm as cm
from astropy.cosmology import FlatLambdaCDM
cosmo = FlatLambdaCDM(H0=70, Om0=0.3)

#reading the table and setting up all the necessary columns
t = Table.read('grg_table.fits')
mosaic_name = 'mosaic.fits'
mosaic = fits.open(mosaic_name)[0]
grglist = Table.read('grg-list.txt',format='ascii')
wise_name = grglist['wise_image']
names = []
obj = []
names = grglist['name']
obj=[]
for i in range(0,63):
    x = names[i].split(',') [0]
    obj.append(x)

#function to find the rms value for each postage stamp
def find_noise(a):
    b=a.flatten()
    for i in range(10):
        m=np.nanmean(b)
        s=np.nanstd(b)
        b=b[b<(m+5.0*s)]
    return m,s

#function to plot all the postage stamps
def GRG(RA,DEC,H_RA,H_DEC,wise,z,output,title):
    Source = {
        'RA' : RA,
        'DEC' : DEC,
        'PixelRes' : 0.00011
    }

```

```

c = SkyCoord(Source['RA'], Source['DEC'], frame='icrs')

nax = 400

wcs_input_dict = {
    'CTYPE1': 'RA---TAN',
    'CUNIT1': 'deg',
    'CDELT1': -Source['PixelRes'],
    'CRPIX1': nax,
    'CRVAL1': c.ra.deg,
    'NAXIS1': 2*nax,
    'CTYPE2': 'DEC--TAN',
    'CUNIT2': 'deg',
    'CDELT2': Source['PixelRes'],
    'CRPIX2': nax,
    'CRVAL2': c.dec.deg,
    'NAXIS2': 2*nax
}

wcs_my = WCS(wcs_input_dict)

wise_file = wise
wise_img = fits.open(wise_file)[0]
wise_reproj = reproject_interp(
    wise_img, wcs_my, shape_out=[2*nax,2*nax], return_footprint=False )
grg_reproj = reproject_interp(
    mosaic, wcs_my, shape_out=[2*nax,2*nax], return_footprint=False )

wcs_mosaic = WCS(mosaic.header, naxis= 2)
wcs_wise = WCS(wise_img.header, naxis= 2)

rms = find_noise(grg_reproj)[1]/1.2
lc = 2.0 * rms
sep = np.sqrt(2.0)
levels = rms * 3.0 * 2**np.linspace(0,15,40)
vmax = np.nanmax(grg_reproj)

plt.clf()
fig = plt.figure(figsize=(8,8))
ax = plt.subplot(projection = wcs_my)

ax.imshow(wise_reproj.data, origin = 'lower',cmap =cm.binary )
ax.contourf(
    grg_reproj.data, levels=levels, cmap=cm.viridis ,alpha=0.6,vmax =vmax)

```

```

ax.scatter(H_RA,H_DEC,transform=ax.get_transform('icrs') ,
marker='X',c='red',s=70, edgecolors='white')

ax.tick_params(axis='both', labelsize=20)
ax.set_xlabel('Right Ascension', fontsize=20)
ax.set_ylabel('Declination', fontsize=20)
ax.set_title(title,fontsize=20)

BarLength_kpc = 500 * u.kpc
redshift = z
kpc_proper_per_arcmin = cosmo.kpc_proper_per_arcmin(redshift)
BarLength_degree = ( BarLength_kpc / kpc_proper_per_arcmin ).to(u.degree)
BarLength_pixel = BarLength_degree / ( Source['PixelRes'] * u.degree )
print(BarLength_pixel)
ax.plot( [2*nax-20-BarLength_pixel,2*nax-20] ,
[20, 20], '- ', lw=5, color='black')
plt.text( 2*nax-20-BarLength_pixel/2, 30, '500 kpc (z=%.3f)'%(redshift),
horizontalalignment='center',color='black', fontsize=12 )

plt.savefig(output,bbox_inches="tight")

#executing the function to obtain postage stamps
for i in range(0,63):
    RA = t[i]['RA'] * u.deg
    DEC = t[i]['DEC'] * u.deg
    H_RA = t[i]['Host_RA'] * u.deg
    H_DEC = t[i]['Host_DEC'] * u.deg
    w_name = wise_name[i]
    z = t['zfinal_new'][i]
    size = 0.02 * u.deg
    title = obj[i]
    img_name = 'GRG_IMG_'+ str(i) +'.png'
    GRG(RA,DEC,H_RA,H_DEC,w_name,z,img_name,title)

```

Acknowledgement

This thesis includes archived data obtained through the CSIRO ASKAP Science Data Archive, CASDA (<http://data.csiro.au>). The Australian SKA Pathfinder is part of the Australia Telescope National Facility (grid.421683.a) which is managed by CSIRO. The operation of ASKAP is funded by the Australian Government with support from the National Collaborative Research Infrastructure Strategy. ASKAP uses the resources of the Pawsey Supercomputing Centre. Establishment of ASKAP, the Murchison Radio-astronomy Observatory and the Pawsey Supercomputing Centre are initiatives of the Australian Government, with support from the Government of Western Australia and the Science and Industry Endowment Fund. We acknowledge the Wajarri Yamatji people as the traditional owners of the Observatory site. This research made use of astropy, a community-developed core Python package for astronomy (Aceituno et al., 2013) hosted at <http://www.astropy.org/> and of TOPCAT (Taylor, 2005).

Declaration of authorship

I hereby declare that the report submitted is my own unaided work. All direct or indirect sources used are acknowledged as references. I am aware that the thesis in digital form can be examined for the use of unauthorized aid and in order to determine whether the report as a whole or parts incorporated in it may be deemed as plagiarism. For the comparison of my work with existing sources I agree that it shall be entered in a database where it shall also remain after examination, to enable comparison with future Theses submitted. Further rights of reproduction and usage, however, are not granted here. This paper was not previously presented to another examination board and has not been published.

Location, date

Signature